molecules

MDPI

Review

Applications of Ferric Oxide in Water Splitting by Electrolysis: A Comprehensive Review

Bruno G. Pollet and Shankara S. Kalanur *

Green Hydrogen Lab (GH2Lab), Hydrogen Research Institute (HRI), Université du Québec à Trois Rivières (UQTR), 3351 Boulevard des Forges, Trois-Rivières, QC G9A 5H7, Canada; bruno.pollet@uqtr.ca
* Correspondence: shankara.kalanur@uqtr.ca

Abstract: In water electrolysis, the use of an efficient catalyst derived from earth-abundant materials which is cost-effective and stable is essential for the economic sustainability of hydrogen production. A wide range of catalytic materials have been reported upon so far, among which Fe_2O_3 stands out as one of the most credible candidates in terms of cost and abundance. However, Fe_2O_3 faces several limitations due to its poor charge transfer properties and catalytic ability; thus, significant modifications are essential for its effective utilization. Considering the future of water electrolysis, this review provides a detailed summary of Fe_2O_3 materials employed in electrolytic applications with a focus on critically assessing the key electrode modifications that are essential for the materials' utilization as efficient electrocatalysts. With this in mind, Fe_2O_3 was implemented in a heterojunction/composite, doped, carbon supported, crystal facet tuned system, as well as in metal organic framework (MOF) systems. Furthermore, Fe_2O_3 was utilized in alkaline, seawater, anion exchange membrane, and solid oxide electrolysis systems. Recently, magnetic field-assisted water electrolysis has also been explored. This comprehensive review highlights the fact that the applicability of Fe_2O_3 in electrolysis is limited, and hence, intense and strategically focused research is vital for converting Fe_2O_3 into a commercially viable, cost-effective, and efficient catalyst material.

Keywords: water splitting; Fe_2O_3; bifunctional catalyst; oxygen evolution reaction; hydrogen

check for updates

Citation: Pollet, B.G.; Kalanur, S.S. Applications of Ferric Oxide in Water Splitting by Electrolysis: A Comprehensive Review. *Molecules* **2024**, *29*, 4990. https://doi.org/10.3390/molecules29214990

Academic Editor: Javier Llanos

Received: 23 September 2024
Revised: 11 October 2024
Accepted: 14 October 2024
Published: 22 October 2024

Copyright: © 2024 by the authors. Licensee MDPI, Basel, Switzerland. This article is an open access article distributed under the terms and conditions of the Creative Commons Attribution (CC BY) license (https://creativecommons.org/licenses/by/4.0/).

1. Introduction

The energy derived from fossil fuels was the main driving force for the industrial and economic growth of the 19th century [1]. At present, roughly 60 to 80 percent of the total energy produced and consumed in developed countries is derived from fossil fuels such as coal, oil, and natural gas, supporting infrastructure systems such as electricity generation and transportation, as well as industry [2]. The past century shows the importance of fossil fuels and energy sources regarding the navigation of human advancement through industrialization and economic growth. However, the extensive usage of fossil fuels poses serious concerns in terms of greenhouse gases (GHG) and pollution, which cause an imbalance in nature, leading to environmental calamities [3]. Moreover, fossil fuels are non-renewable and geopolitically controlled natural resources which pose challenges in terms of constant extraction and controlled supply chains; thus, their replacement is inevitable [4]. Importantly, a profound shift toward carbon-free, renewable, and sustainable energy resources is essential in terms of safeguarding the environment and supporting economic stability along with industrial growth. Hence, the current focus of research presents an unprecedented opportunity to regulate global warming via the development of carbon-neutral technologies.

Among the currently available green (or renewable) energy contenders, hydrogen has been found to be the ideal option to replace fossil fuels [5]. The abundance of atomic and molecular hydrogen on Earth in a wide range of naturally available molecules such as water, fossil fuels, etc. makes it a potential candidate as a future renewable energy source [6]. The

superiority of hydrogen as a source of energy compared with other sources is due to its extensive utilization in wider applications that provide energy (heat/electricity) with a high specific energy density [7] and to the fact that it releases carbon-free water as a byproduct, e.g., when used in fuel cells [8–10]. Hence, the demand for hydrogen is significantly increasing and is expected to continue to rise in the coming decades owing to industrial applications in addition to applications in energy infrastructure. The availability and green production of hydrogen in all parts of the globe (water), combined with sustainable routes of extraction, make it an ideal energy source for energy independence, regardless of geopolitical situations. Given its advantages and demand, the extensive research advancements in hydrogen-driven energy and industrial utilization could experience exponential growth due to the commitment of major economic players to shift toward carbon-free technologies.

Advancement toward a hydrogen infrastructure has gained significant attention and funding recently, as it plays an important role in achieving the Paris Agreement target set for the reduction in emissions by 2050 [11]. To achieve this target, reducing the cost of hydrogen is crucial; this depends on hydrogen production technologies, storage, transportation, and utilization. Recent developments reveal that the rapid and onsite/remote availability of hydrogen from a wide range of production technologies is capable of significantly reducing storage and transportation expenses. However, the choice of suitable hydrogen production technologies is a vital factor that influences the overall cost of hydrogen (LCOH—levelized cost of hydrogen). Figure 1 represents the various types of hydrogen produced around the globe, along with their sources of production and the amount of carbon emissions associated with these production technologies. Note that, except for green hydrogen, other methods of hydrogen production (black, blue, brown, and grey) use fossil fuels as a source of hydrogen; only green hydrogen uses water as a source (if renewables and water electrolysis are used). Moreover, except for blue and green hydrogen technologies, all other methodologies emit enormous amounts of GHG and are thus not recommended as sources of energy in the future. Notably, the reduction in carbon emissions (such as carbon dioxide, CO_2) for blue hydrogen is due to the carbon capture and sequestration (CCS) processes linked to those hydrogen production systems.

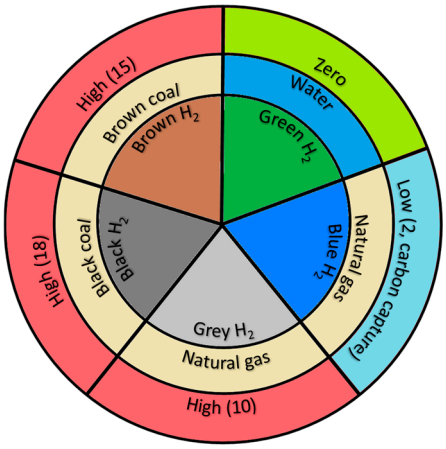


Figure 1. Types of hydrogen (green, blue, grey, black, and brown hydrogen) produced (first circle) around the globe, along with their sources (second circle) and their carbon emission levels (third circle). Approximate values of $kgCO_2/kgH_2$ produced are indicated.

Among large-scale hydrogen production technologies, the steam methane reforming (SMR) method dominates as the most cost-effective production technology (>99%) [12]. However, the utilization of fossil fuels in SMR leads to enormous carbon emissions. Even though SMR technology could be converted to blue hydrogen by combining it with CCS, its dependence on fossil fuels makes it a geopolitical challenge and expensive (due to carbon capture processing) compared to the other technologies. Therefore, the use of carbon-free sources and methods, along with the use of renewable energy, is essential for achieving

cost-effective, pilot-scale hydrogen production in order to fulfil the emission target and achieve cost reductions. In particular, rigorous research and development are essential to explore, develop, and exploit greener hydrogen production technologies that could meet future demands and are cost effective.

2. Overview of Electrochemical Water Splitting

Electrochemical water splitting is a process of water oxidation and reduction to produce O_2 and H_2 under an applied potential bias/electricity, as shown in Equation (1). The phenomenon of the decomposition of molecules using an applied current was first observed in 1789 and was later applied to in water electrolysis in 1800 by Nicholson and Carlisle [13]. Later, water electrolysis methodology was optimized and further developed into a mature technology for increased efficiency and practicality. Recently, the importance of water electrolysis has gained significant attention, given that it is carbon-free approach to hydrogen production utilizing renewable and sustainable resources. For electrolysis, the water required for H_2 and O_2 production could be sourced from the sea or any water body, and electricity generated using green and inexpensive renewable sources, such as solar and wind, could provide the required electrical energy to split the water molecules. Thermodynamically, the energy required to split water into H_2 and O_2 is shown in the below equation.

$$H_2O + \text{Electricity (237.2 kJ mol}^{-1}) + \text{Heat (48.6 kJ mol}^{-1}) \rightarrow H_2 + \tfrac{1}{2}\,O_2 \quad (1)$$

The above equation represents an ideal condition required in terms of the energy, electrodes, and charge dynamics required to split water into H_2 and O_2. Electrochemically (thermodynamic cell voltage), a minimum bias voltage of 1.229 V vs. a standard hydrogen electrode (SHE) is required to oxidize water at the anode to produce O_2 and to produce H_2 gas at the cathode surface. However, under normal experimental conditions, the required voltage has been found to be higher than the theoretical values (>1.229 V vs. SHE) to overcome the ohmic resistance of the electrolyte and the reaction kinetics in the electrochemical cell. The process of water electrolysis in an electrochemical cell is shown in Figure 2. To split water, the electrode materials are connected to the anode and cathode supply of the power output and are immersed in a suitable electrolyte. Under the applied electricity, the water molecules are split into O_2 via oxygen evolution reaction (OER) and H_2 through hydrogen evolution reaction (HER) at the anode and cathode surfaces, respectively. Generally, the anode and cathode compartments are separated using a separator/diaphragm/membrane to avoid the mixing of H_2 and O_2 gases and to maintain the flow of ions between the compartments.

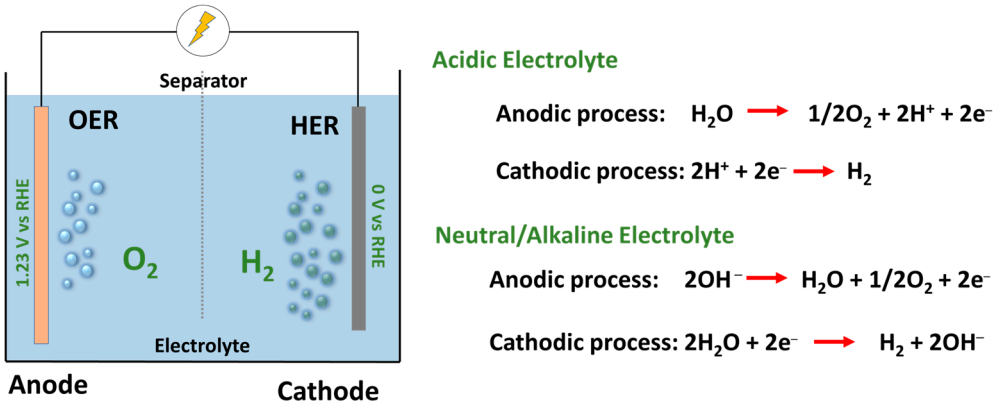


Figure 2. Schematic presentation of electrochemical water splitting (electrolysis) under acidic, neutral, and alkaline conditions.

Water electrolysis can be achieved in a wide range of electrolytes of different pH values with the utilization of efficient and stable electrodes. In acidic electrolytes, the water is oxidized at the anode surface, which gives two electrons, whereas the H^+ ions are diffused through the separator/membrane toward the cathode to combine with electrons to yield H_2 gas. In neutral and alkaline electrolytes, OH^- ions are consumed to produce O_2 gas along with two electrons and a water molecule, which are reduced to H_2 at the cathode surface with the release of OH^- ions. The constant production of H_2 and O_2 is balanced by the production and diffusion of the relevant ions toward the respective electrode surface (Figure 2). In water electrolysis, the use of electrolytes is essential to provide significant conductivity between the electrodes, i.e., to decrease the ohmic resistance and create a feasible ionic environment at the electrode surface for effective OER and HER activity. Hence, the utilization of electrolytes with high ionic mobility is essential to decrease the thermodynamic barrier and energy requirement to oxidize and reduce water molecules. Generally, potassium hydroxide (KOH), sulfuric acid (H_2SO_4), sodium sulfate (Na_2SO_4), phosphate buffers, etc. are used as electrolytes in the water electrolysis systems.

3. Electrolysis Techniques

Electrolysis techniques are generally classified based on the setup and components utilized, as shown in Figure 3, among which alkaline water electrolysis (AWE), proton exchange membrane water electrolysis (PEMWE), anion exchange membrane water electrolysis (AEMWE), and solid oxide electrolysis cells (SOECs) are the most widely used methods (Figure 3). In AWE, the anode and cathode half-cell reactions take place (under the applied cell potentials) in different compartments separated by diaphragms/separators that allow the effective diffusion of OH^- ions from the cathode (after HER) to the anode side to carry out the OER process. AWE is generally operated with very high pH electrolytes (up to 5–7 M) using Ni-based electrodes. Due to its simplistic design and minimal component requirements, AWE is widely used in hydrogen production at pilot/industrial scales. In PEMWE, the anode and cathode sides are separated by a PEM (usually Nafion®), which facilitates the effective diffusion of H^+ ions. During the electrolysis, the water molecules are oxidized at the anode side, producing H^+ ions that are transferred to the cathode side via the PEM for the water reduction reaction. For the electrolysis, acidic electrolytes are passed through the anode side containing an OER (iridium dioxide, IrO_2) catalyst. At the cathode side, platinum (Pt) nanoparticle-supported on carbon black (Pt/C) catalysts are widely employed as electrodes for HER processes. The PEM setup involves the use of gas diffusion layers (GDL), which yield high-purity H_2 compared to that produced using AWE.

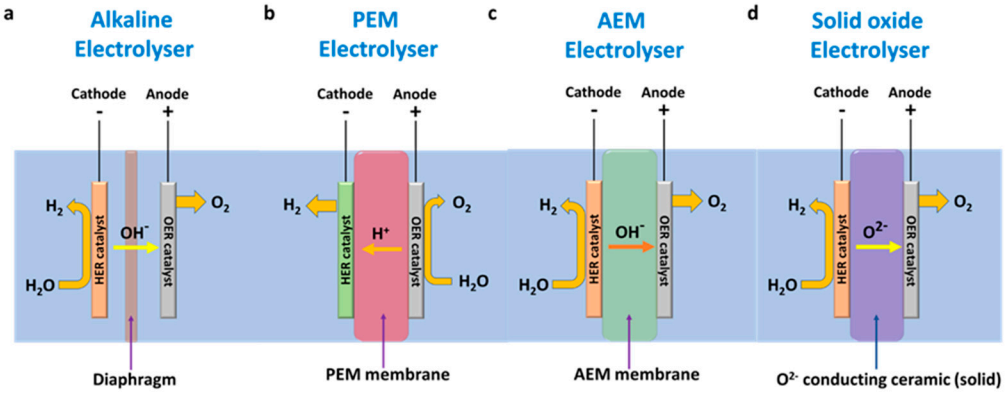


Figure 3. Schematic presentation of different types of electrolyzers: (**a**) alkaline water electrolyzers, (**b**) PEM electrolyzers, (**c**) AEM electrolyzers, and (**d**) solid oxide electrolyzers.

The AEMWE was developed by combining the advantages of AWE and PEMWE. The AEMWE is a membrane-based alkaline electrolyzer that produces high-purity H_2 in mild basic conditions without the use of platinum group metal (PGM) catalysts. During electrolysis, the basic electrolyte is fed into both the anode and cathode side to produce H_2, whereas the OH^- ions diffuse toward the anode through the AEM to generate O_2. Recently, AEMWE has demonstrated promising breakthroughs, indicating its commercial viability and pilot-scale production capability. SOEC systems are operated at very high temperatures (>700 °C) to split water into O_2 and H_2. At elevated temperatures, the water is fed in the form of steam at the cathode side, where H_2 is produced. A solid ceramic membrane was used to separate the anode and cathode sides, allowing the effective diffusion of O^{2-} ions from the cathode to the anode cell. Similar to AEMWE, SOEC has exhibited promising commercial viability, indicating its potential contribution to hydrogen production in the future.

In water electrolysis systems, the catalysts and electrodes employed for OER and HER activities play a vital role in determining the overall efficiency, stability, and long-term operation potential. Noble metals (PGMs) are widely known for their efficient catalytic activity toward OER and HER and thus are routinely used in commercial and pilot-scale electrolyzers. In particular, the noble metals show significantly low overpotential (η) to split water into H_2 and O_2 in comparison to the non-noble metal catalysts. Hence, a non-noble metal catalyst needs comparatively higher overpotentials to perform OER and HER. Despite the efficiency factor, the cost, abundance, and geographical conditions need to be considered for commercial acceptance, along with cost reductions. Hence, catalysts derived from non-noble metals are recommended, as these are cost-effective, abundant, and stable. With this in mind, the catalysts/electrodes play a crucial role in determining the hydrogen production cost, and thus, the viability of commercial hydrogen. However, non-noble catalysts show limited catalytic activity, and thus, various modifications and different strategies are essential [14–16] for their effective implementation in electrolyzers. Therefore, the choice of a suitable catalyst and the required modifications are critical in developing efficient catalysts for water splitting in electrolyzers.

4. Fe_2O_3

The use of metal oxides in OER processes is known to be an effective approach, as the surface of metal oxides (MOx) provides essential sites for reaction intermediates to be adsorbed to initiate OER activity. Specifically, the adsorption and desorption of essential reaction intermediates on the metal oxide surface is an important step toward achieving water splitting reactions. Reaction intermediates with optimum adsorption energies at the oxide surface hold the key to improving water splitting efficiency [17]. Moreover, the conductive nature of MOx means that it serves as an effective charge diffusion/transfer medium. MOx can be obtained with different nanostructures, crystal phase/planes, and doped, and it can be anchored to a wide range of catalysts/substrates. Hence, the use of MOx in electrocatalytic processes offers a promising strategy for hydrogen production. Among metal oxides, Fe_2O_3 is an abundant mineral form of Fe metal (in addition to other minerals) in nature. The hematite mineral form of Fe_2O_3 is the naturally occurring form of iron, a known primary element extracted from the earth's crust. In general, Fe_2O_3 has a dark red or brown color and has various polymorphs. Fe_2O_3 is known for its relatively weak ferromagnetic properties at room temperature; it also exhibits antiferromagnetic properties below 260 K. Even though the magnetic properties of Fe_2O_3 are not known to directly influence its other applications, they have been found to affect its carrier transport properties and optoelectronic characterizations, owing to the various spin configurations. Furthermore, Fe_2O_3 exhibits strong photon absorption in the visible yellow region to UV, with a photon transmission in the orange to the infrared region that results in the typical red

appearance. Fe_2O_3 has a band gap of 2.1 eV, which accounts for the absorption of ~40% of sunlight and thus presents semiconductor properties. Fe_2O_3 is highly stable and can be easily dissolved/reacted with most acids. The other forms of iron oxides generally found in nature are FeO (iron (II) oxide) and Fe_3O_4 (magnetite). Due to its abundance, cost, absorbance, stability, and non-toxic nature, Fe_2O_3 is effectively utilized in a wide range of applications [18], including as an anode material in batteries [19], in supercapacitors [20], in gas-sensing [21], in electrochemical sensors [22], for photoelectrochemical water splitting [23], dye degradation [24], in biomedical applications [25], and in electrolysis [26]. In particular, considering its OER capabilities under the applied bias potential (with or without illumination), Fe_2O_3-based electrodes have been used for water-splitting applications using both photoelectrochemical [27] and electrocatalytic modes [28]. Furthermore, Fe_2O_3 has been effectively employed in biomedical applications due to its superior permeability and stability. In particular, Fe_2O_3 has been utilized to transfer therapeutic agents through tissues and in controlled drug-releasing agents. Due to its non-toxic nature, Fe_2O_3 is well suited as nano-carriers for drugs that could limit and regulate the drug dosage and supply, resulting in more effective treatments. The utilization of Fe_2O_3 in medicine offers effective treatments for drug release and limits overdosages to certain body sites. Recent work on Fe_2O_3 applications has led to Fe_2O_3 being recognized as a superior catalyst molecule when employed directly and as a support material. Owing to its unique physiochemical properties, two different valence oxidation states, and surface properties, Fe_2O_3 is being effectively employed in energy applications. Therefore, the use of Fe_2O_3-based materials as electrodes, photoelectrodes, and catalysts could provide a promising opportunity for cheap hydrogen production technologies.

Fe_2O_3 is found in α-, β-, γ-, and ε- polymorphs, having different properties and stabilities. Among the polymorphs, the α phase has been widely studied owing to its stability and feasible application in charge storage devices and as pigments in paints [29,30]. β-Fe_2O_3 contains a bixbyite structure and is a rarely studied polymorph due to its intermediary metastable condition, which transforms to α-Fe_2O_3 at higher temperatures [31]. The γ polymorph of Fe_2O_3, also known as maghemite, contains a cubic structure and shows ferromagnetic properties [32]. The ε-Fe_2O_3 polymorph is a well-known magnetic material exhibiting a non-centrosymmetric orthorhombic structure [33]. Among the polymorphs, both α and γ show interchangeable crystalline forms, in which α-Fe_2O_3 becomes dominant and stable at higher temperatures when treated in an inert atmosphere and with a reducing agent [34].

Hematite (Fe_2O_3) is commonly described as having a hexagonal crystal structure. However, the fundamental crystal system is found to have a rhombohedral structure, that is, a hexagonal unit cell with specific parameters is used to describe the rhombohedral lattice of hematite Fe_2O_3. A typical crystal structure of hematite Fe_2O_3 is presented in Figure 4 (generated using Vesta [35]). The rhombohedral crystal system of hematite shows $\overline{R}3c$ space groups which could be transformed and described using hexagonal coordinates. Note that even though the underlying crystal structure of hematite Fe_2O_3 is rhombohedral, it is often described in terms of a hexagonal lattice system for convenience, as shown in Figure 4. In hematite α-Fe_2O_3 having $\overline{R}3c$ space group, six equivalent O^{2-} atoms are bonded to one Fe^{3+} atom to form FeO_6 octahedra, whereas the lattice O^{2-} ions appear to be bonded to four equivalent Fe^{3+} atoms. The O^{2-} atoms bonded to Fe^{3+} form a mixture of distorted edge and corner-sharing OFe_4 trigonal pyramids, as shown in Figure 4, whereas the FeO_6 octahedra is found to form an edge and corner-sharing, along with a distorted face configuration with the neighboring octahedra.

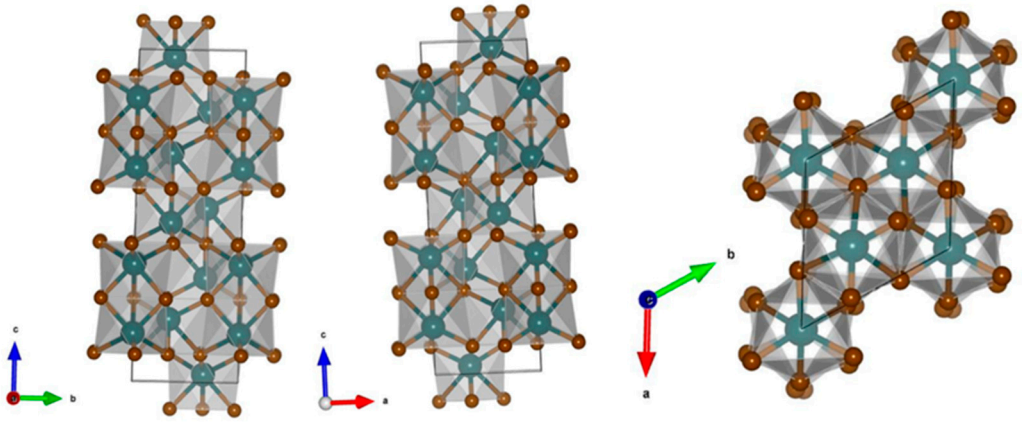


Figure 4. Crystal structure of α-Fe_2O_3 having a rhombohedral system of $\overline{R}3c$ space groups, showing a trigonal-hexagonal scalenohedral geometry.

4.1. Water Splitting Applications of Fe_2O_3

Recently, Fe_2O_3 has been extensively used in water-splitting applications in both photoelectrochemical and electro-catalytical modes. Among the widely explored transition metals, Fe demonstrates considerably superior electrocatalytic activity, including HER, OER, and the oxygen reduction reaction (ORR), even compared to widely used Co and Ni-based materials [36–38]. Owing to its valency between the (III) and (II) states that offers exceptional catalytic properties and stability in comparison with the Ni and Co-based metal oxides, Fe possesses a feasible reversible redox capability [39]. Figure 5a shows the number of research articles published (photoelectrochemical and electrocatalytic modes) on the use of Fe_2O_3 electrodes for water splitting in recent decades. A gradual increase in the number of articles indicates that Fe_2O_3 is gaining significant attention owing to its semiconductor and catalytic properties. The extensive utilization of Fe_2O_3 in photoelectrochemical and photocatalytic applications is evident, owing to its absorbance and band edge properties that facilitate OER activity using photogenerated charges. Figure 5b shows the number of articles published during the last decade concerning the electrocatalytic water-splitting activity of Fe_2O_3, indicating the importance of Fe_2O_3 in water-splitting applications. In electrocatalytic water splitting systems, Fe_2O_3 materials with relevant modifications, including heterojunction with oxides/carbon/hydroxide/MOF systems, doping, oxygen vacancy tuning, etc., have been employed. In addition, Fe_2O_3 has exhibited significant activity as a catalyst in AEM and SOEC systems. Table 1 shows the literature reports on Fe_2O_3 in electrocatalytic water splitting applications. Additionally, the sections below provide a detailed discussion of various catalytic activity and electrochemical characterizations.

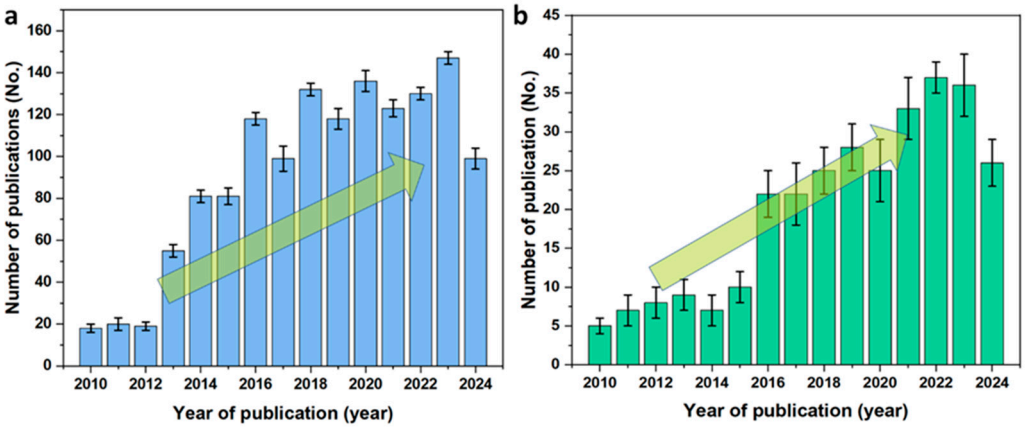


Figure 5. Articles on Fe_2O_3 for (**a**) water splitting (including solar, electrochemical, and photoelectrochemical routes) and (**b**) electrocatalytic water splitting.

Table 1. Fe_2O_3 electrodes employed in electrolysis and their experimental and electrochemical properties.

Catalyst/Electrode	Synthesis Method	Electrolyte	Stability	Overpotential mV vs. SHE	Tafel Slope (mV dec^{-1})	Ref
Ni and Zn-doped Fe_2O_3	Combustion method	0.1 M KOH	-	OER: 350 (for 10 mA cm^{-2})	OER: 26	[40]
Se-Fe_2O_3@Ni/NiO	Thermal method	1 M KOH	21 h	OER: 205 (for 10 mA cm^{-2})	OER: 36	[41]
P-doped Fe_2O_3/ZnO	Chemical bath deposition/hydrothermal/CVD	1 M KOH	24 h	OER: 250 HER: 139 (for 10 mA cm^{-2})	OER:40 HER: 66	[42]
Zn and S co-doped Fe_2O_3	Hydrothermal/CVD	1 M KOH	100 h	OER: 350 (for 500 mA cm^{-2})	OER: 47.5	[43]
Co_3O_4/Fe_3O_4	Co-precipitation method	0.1 M KOH	8 h	OER: - HER: -	OER: 62 HER: 102	[44]
C-doped $CoFe_2O_4/Fe_2O_3$	Calcination approach	1 M KOH	5.5 h	OER: 260 HER: 236 (for 20 mA cm^{-2})	OER: 183 HER: 146	[45]
$CoMo/Fe_2O_3$	Hydrothermal/ Electrodeposition methods	1 M KOH	100 h	OER: 266 HER: 71 (for 10 mA cm^{-2})	OER: 54 HER: 85	[46]
Fe_2O_3@CuO	Hydrothermal	1 M KOH	25 h	OER: 230 HER: 130 (for 10 mA cm^{-2})	OER: 54 HER: 77	[47]
IrO_2–Fe_2O_3	Thermal decomposition	0.5 M H_2SO_4	600 cycles	HER: 78 (for 10 mA cm^{-2})	HER: 36.2	[48]
RuO_2–Fe_2O_3	Synthesis thermal treatment	1 M KOH	-	OER: 292 (for 500 mA cm^{-2})	OER: 56.08 HER: −43	[49]
RuO_2/Fe_2O_3	Synthesis	1 M KOH	18 h	OER: 386 HER: −239 (for 10 mA cm^{-2})	OER: 67 HER: 97	[50]
Fe_2O_3@NiO	Hydrothermal	1 M KOH	20 h	OER: 224 HER: 187 (for 10 mA cm^{-2})	OER: 20 HER: 53.8	[51]
WO_3/Fe_2O_3-NiO	Chemical etching reaction and decomposition	1 M KOH	100 h	OER: 211 (for 100 mA cm^{-2})	OER: 39.5	[52]
$Fe_2O_3/Ni(OH)_2$	Electrodeposition	1 M KOH	18 h	OER: 291 (for 10 mA cm^{-2})	OER: 53.7	[53]
Ni_1Fe_2@Fe_2O_3@C	High-temperature calcination	1 M KOH	30 h	OER: 271 (for 10 mA cm^{-2})	OER: 78	[54]
Fe_2O_3-MnO	Sol-gel method	1 M KOH	1000 cycles	OER: 370 (for 10 mA cm^{-2})	OER: 66	[55]
Fe_2O_3|||FeP	Electrochemical oxidation/solution self-assembly/pyrolysis	1 M KOH	20 h	Hydrazine overpotential: 0.61 V HER: 138 (for 10 mA cm^{-2})	OER: 179.2 HER: 63.9	[56]
Fe_2O_3/FeP	Hydrothermal	1 M KOH	12 h	OER: 264 (for 10 mA cm^{-2})	OER: 47	[57]
Fe_2O_3/FeS	Hydrothermal	1 M KOH	10 h	OER: 264 (for 40 mA cm^{-2})	OER: 90	[58]
FeS/Fe_2O_3	Chemical etching/solvothermal	1 M KOH	10 h	OER: 266.5 (for 10 mA cm^{-2})	OER: 51.17	[59]
Fe_2Se_3/Fe_2O_3	Synthesis	1 M KOH	24 h	OER: 160 (for 20 mA cm^{-2})	OER: 30.02	[60]
Fe_2O_3/CNT	Co-precipitation method	1 M KOH	12h	OER: 383 (for 10 mA cm^{-2})	OER: 62	[61]
Fe/Fe_2O_3-Fe-N-doped C	Pyrolysis	0.1 M KOH	10h	OER: 0.69 V vs Ag/AgCl (for 10 mA cm^{-2})	OER:77.5	[62]
Fe_2O_3/g-C_3N_4	Thermal method	0.5 M KOH	10 min	OER: 425 (for 10 mA cm^{-2})	OER: 280	[63]
Fe_2O_3-C	Pyrolysis	1M KOH	48 h	HER: 245 (for 10 mA cm^{-2})	HER: 76.6	[64]
Ni_3S_2/Fe_2O_3/ N-doped carbon	Thermal process/CVD	1 M KOH	200 h	OER: 188 (52 mA cm^{-2}) HER: 78 (10 mA cm^{-2})	OER: 64.3 HER: 115.8	[65]

Table 1. *Cont.*

Catalyst/Electrode	Synthesis Method	Electrolyte	Stability	Overpotential mV vs. SHE	Tafel Slope (mV dec^{-1})	Ref
Fe_2O_3/N-graphene	Co-deposition (hydrothermal and electrodeposition)	1 M KOH	22 h	OER: 313 (for 100 mA cm^{-2})	OER: 81	[66]
Fe_2O_3/MWCNT	Pulsed laser ablation	1M KOH	10 h	OER: 310 (for 10 mA cm^{-2})	OER: 20.35	[67]
MOF-Fe_2O_3	Solvothermal	1 M KOH	20 h	OER: 439 HER: 230 (for 10 mA cm^{-2})	OER: 99 HER: 100	[68]
Fe_2O_3/NiO	Chemical bath deposition	1 M KOH Sea water Domestic sewage	50 h	OER: 182 (for 10 mA cm^{-2}) OER: 291 (for 1 A cm^{-2}) OER: 329 (for 1 A cm^{-2})	OER: 45	[69]
P-Fe_2O_3-CoP	Hydrothermal-gas-phase phosphorization process	Freshwater Seawater	12 h	OER: 250 HER: 219 (for 10 mA cm^{-2}) OER: 270 HER: 152 (for 10 mA cm^{-2})	OER: 42 HER: 79 OER: 59 HER: 95	[70]
RuNi-Fe_2O_3/IF	Hydrothermal	1 M KOH 1 M KOH + seawater	100 h	OER: 329 HER: 75 (for 100 mA cm^{-2}) OER: 424 HER: 298 (for 100 mA cm^{-2})	OER: 60.85 HER: 85.08 OER: 69.58 HER: 114.31	[71]
Co-Fe_2O_3 (AEM)	Microwave-assisted hydrothermal	1.0 M KOH	500 h	OER: 310 (for 10 mA cm^{-2})	OER: 29	[72]

4.2. DFT Studies on the OER Activity of Fe_2O_3

Density functional theory (DFT) calculations offer a powerful tool to provide significant information regarding the surface and intrinsic properties of different elements/materials. In the case of Fe_2O_3, different surface orientations/crystal planes exhibit different atomic arrangements, distance defects, and atom densities which, in turn, affect their electronic structure and reactivity. Specifically, the adsorption of OER intermediates, their catalytic nature, and the stability of different facets/planes demonstrate important parameters in determining the efficiency of the water splitting. With this in mind, a wide range of DFT studies have been reported, highlighting the effects of different facets and their OER activities. Mainly, the (0001) facet of Fe_2O_3 has been reported to be more favorable for OER compared to other facets. The OER activity on the (0001) facet of completely hydroxylated Fe_2O_3 favors [73] the effective adsorption of reaction intermediates, resulting in enhanced OER activity. Furthermore, the doping of Fe_2O_3 (containing a fully hydroxylated surface) at the Fe and O sites using metal ions and anions, respectively, shows improved activity. For example, Ni and Co doping in Fe_2O_3 lead to the formation of a thermodynamically favored surface for effective adsorption reaction intermediates and increased efficiency of OER activity, resulting in low overpotentials. In-depth studies have indicated that active anion dopants at O lattice sites could improve the stability of the holes [73]. Furthermore, the surface states present at the (0001) facet of Fe_2O_3 have been found to affect the OER activity. The formation of a stable peroxo Fe-O-O-Fe adsorbate at the Fe_2O_3 surface has been found to be possible, whereas the presence of a Fe-O· type bond could be effective and is one of the possible intermediate pathways for the OER activity at the (0001) surface [74].

Similarly, DFT studies performed on the different exposed facets of Fe_2O_3 [75] have indicated a specific favorable OER orientation. Several facets of Fe_2O_3 have been studied, including (211), (021), (101), (210), and (100), which have, in general, been found to be less dominant in terms of OER activity. The calculations were performed by considering the free energy and overpotential values that dictate the four electron-coupled electron transfer reactions with OER intermediates. Studies revealed that the different orientations showed different free energy and overpotential values owing to the activity of intermediate species adsorbing on the facets, resulting in varied stability concerning the free energy values, which affects the resulting OER performance. Specifically, the orientation of Fe_2O_3

along (100) has been found to show relatively decreased overpotential values compared to the (211), (021), (101), and (210) orientations. Notably, the surface site in Fe_2O_3 that is responsible for the bridging of two Fe atoms on the (100) surface is favorable for adsorbate interactions, leading the enhanced OER activity. Interestingly, the (110) facet of Fe_2O_3 is known to be one of the favorable orientations for OER activity, as demonstrated by Zhang et al. [76] because, at the (100) facet, a noticeable competing OER reaction intermediate was observed at a single site between the O-O coupling and the formation of OOH. Here, O–O coupling refers to the involvement of two adjacent terminal Os at a dual site, leading to O–O bond formation. Furthermore, the presence of oxygen vacancies plays a critical role in decreasing the OER overpotentials [76]. Conclusively, DFT studies have indicated that the possible reaction pathways and favorable facets of Fe_2O_3 could be modified via the surface state, vacancies, and doping.

4.3. Crystal Facet and Morphology Tuning in Fe_2O_3

The morphology and the exposed crystal plane of Fe_2O_3 have a significant influence on the OER activity [77]. Generally, the interpretation of the structure−activity of electrodes/catalysts is cumbersome when analyzed using conventional electrochemical techniques. In most cases, interpretations of the results have been based on the average activity rather than a specific site or plane of activity, yielding an unambiguous conclusion. Therefore, for better clarity and more accurate interpretations, the direct mapping of electrochemical activities on the isolated crystals is essential. Using scanning electrochemical cell microscopy, Li et al. [77] proposed a single-entity electrochemical strategy to investigate the site-specific OER activity of Fe_2O_3. In their study, a single nanorod crystal of Fe_2O_3 was considered to monitor the OER activity; heterogeneity between and within the single nanorod crystal was observed. The single crystal Fe_2O_3 nanorods were obtained using the hydrothermal method. The produced nanorods has 0.5–1.5 μm rod lengths with a width of ~150 nm. The high-resolution morphology study confirmed significant electrochemical activity owing to the {001} plane present in the nanorod body. Accordingly, the enhanced OER activity was recorded at the {100} facet at the tip, which exhibited significantly increased activity. Hence the facet-dependent OER activity indicated that producing longer Fe_2O_3 nanorods with desired exposed facets would be beneficial compared to the other morphologies. Importantly, the proposed single-entity and sub-entity mapping strategy were shown to be an effective route to explore the intrinsic, surface, and facet-dependent catalytic activity; this approach could be broadly extended to other metal oxide nanostructures. The most important aspect of that study was the interpretation of the structural characteristics of most reactive OER sites on the surface of Fe_2O_3, which is crucial to optimize and engineer catalytic properties which could be applied to electrolyzers. Within the framework of a nanostructure, a crystal plane with active reactive sites is the key that needs to be recognized by engineering a specific nanoarchitecture which is generally hidden, shadowed, or removed/decreased in scale due to the presence of other nonreactive sites/planes.

4.4. Doped Fe_2O_3 Catalysts

The properties of metal oxides can be tuned/engineered to enhance electrochemical properties by introducing cations/anions into the crystal via doping [78]. In the case of Fe_2O_3, the intrinsic and surface properties could be altered/modified by doping. Generally, doping is achieved using a cation or an anion (or both) that displaces Fe or O atoms in the lattice. Doping could be performed during the synthesis process or in subsequent steps at high temperatures that ensure the effective displacement of Fe or O atoms from their lattice locations. The strategy of doping has advantages for materials like Fe_2O_3, which are abundant and cheap materials that show poor catalytic properties in their base form. Based on the nature of the dopant material, the properties of Fe_2O_3 could be tuned/engineered for optimum efficiency. For example, the utilization of Ni or Zn as a redox and non-redox active species, respectively, has been found to have a significant influence on the catalytic activity

of Fe_2O_3, as noted by Shah et al [40]. Pristine and doped (Ni and Zn) Fe_2O_3 were obtained using a flame combustion method, followed by ball milling at 25 Hz for 15 min. Even though Ni is known to be effective as a dopant, Zn doping in Fe_2O_3 yielded significantly higher electrocatalytic properties. A low overpotential value of 350 mV was observed to reach 10 mA cm^{-2}. The experimental and theoretical calculations indicated that the Ni dopant sites had a redox characteristic, whereas the Zn dopant sites on Fe_2O_3 showed a non-redox characteristic. With this in mind, Ni tends to lower the energetic barrier of the OER process, resulting in improved catalytic activity compared to pristine samples. However, in the case of Zn doping, a unique reaction pathway was observed, which is termed as proton-coupled electron transfer; this approach is thermodynamically favored and thus showed enhanced OER activity. Pristine F_2O_3 offers routine four-electron oxidation reaction sites, while Zn-Fe_2O_3 provides a rapid and effective reaction site that utilizes efficient two-site reaction pathways. Here, the Zn site was shown to possess a non-redox characteristic, as it maintained a constant charge during the water oxidation process.

Based on the nature of the dopant, doping amount, and site, a significant alteration of the surface and bulk properties of Fe_2O_3 could be achieved. For example, the doping of Se in Fe_2O_3 linked to Ni/NiO particles was reported to show efficient OER activity [41]. The synthesis of Se-doped Fe_2O_3 on a Ni/NiO nanostructure was achieved using a thermal method that supported in situ deposition directly on carbon fibers. The formation of a solid solution was not observed in the proposed method due to the limited etching of Fe to the carbon support, leading to the doping of Se in Fe_2O_3 that inhibited the diffusion to Ni system to form Se-Fe_2O_3-Ni/NiO. This characterization indicated that the employed technique successfully incorporated nanoparticles of Se-Fe_2O_3-Ni/NiO into the porous structure of the carbon fiber. LSV measurements performed in 1M KOH indicated the production of 10 mA cm^{-2} current density at an impressively lower overpotential value of 205 mV for the OER. Furthermore, a low Tafel slope of 36 mV dec^{-1} was recorded, with a low charge transfer resistance at the electrolyte interface. The superior conducting property of the carbon substrate and the systematic arrangement of Fe_2O_3@Ni/NiO nano junction systems in the porous carbon substrate structure, along with favorable interfaces (Se-Ni/NiO and Se-Fe_2O_3), led to an impressive electrochemical result, confirming the efficient OER activity of the Se-Fe_2O_3-Ni/NiO electrode.

The introduction of nonmetal/anion dopants into a Fe_2O_3 lattice is known to improve its electrocatalytic properties [79]. Unlike doping with Se, doping with P transforms Fe_2O_3 into an efficient bifunctional catalyst which has been utilized only as an OER catalyst [42]. Previous studies have shown that the introduction of PO_4 into Fe_2O_3 improves the catalytic activity; this could be synthesized by performing electrochemical cycles in phosphate buffers [80]. The doping of P in iron oxides is known to regulate the electrical properties [79,81] which, in turn, effects the electrocatalytic efficiency. Generally, a support material is required for Fe_2O_3 owing to its limitation regarding the mass transfer process. In such a case, different metal oxides and morphologies have been adopted as support materials for the Fe_2O_3 catalyst. For example, the utilization of ZnO nanotubes as a support material for P–Fe_2O_3 is known to boost the catalytic activity, as the 1-dimensional tube structure of the support oxides (ZnO) provides effective pathways for the charges. On the other hand, the doping of Fe_2O_3 by anions such as P has been found to increase the donor density and improve the charge transfer process. A ZnO-coated P-Fe_2O_3 nanostructure was fabricated using chemical bath deposition (ZnO nanotube), followed by solution processing (Fe) and chemical vapor deposition (for P doping). During the water splitting experiments, ZnO-coated P-Fe_2O_3 generated 10 mA cm^{-2} of current density at low OER overpotential at 250 mV, whereas the HER overpotential was observed at 139 mV. The applicability of ZnO/P-Fe_2O_3 was evaluated by testing the overall water splitting in two electrode systems, in which the HER and OER processes were effectively performed at a lower bias potential of 1.62 V. Furthermore, the prolonged electrolysis ability of the electrode over six days was established, indicating the stability and versatility of the ZnO-coated P-Fe_2O_3 bifunctional catalyst. Similarly, P-doped Fe_2O_3 linked to CoP was also explored for overall water

splitting, including seawater electrolysis (discussed in later sections). Liu et al. [43] demonstrated the doping of both anion and metal ions into Fe_2O_3 for enhanced water-splitting applications. Zn was used as a cation, whereas S was employed as an anion dopant, which was simultaneously introduced into Fe_2O_3 linked to Fe_3O_4 on the iron foam. The Zn and S doped-Fe_2O_3/Fe_3O_4 (on iron foam) was found to undergo directional reconstruction into FeOOH to transform into Zn and S doped-Fe_3O_4-FeOOH (on iron foam). Even though Zn/S/Fe_3O_4-FeOOH showed the highest OER efficiency, its Fe_2O_3 counterpart showed significant water-splitting efficiency. Conclusively, doping Fe_2O_3 by anions and/or metal ions seems to be the key to enhancing the water-splitting activity and stability.

4.5. Fe_2O_3 in Heterojunction Systems

Constructing a heterojunction system with Fe_2O_3 offers significant advantages, e.g., providing support to the catalyst, acting as the main catalyst to support active sites, providing oxygen-deficient defects, etc., thereby improving the electrocatalytic activity. Specifically, the utilization of Fe_2O_3 as a support material for the catalyst is expected to decrease the quantity of loading of the main catalyst, which becomes vital in the case of expensive and rare metal-based catalysts. For example, the loading of a Co_3O_4 catalyst could be significantly reduced by using Fe_2O_3 as a support [44]. Even though experimental results have shown that Fe_3O_4 acts as a superior support to Co_3O_4 compared to Fe_2O_3, it still behaves more efficiently than the base Fe_2O_3 and Co_3O_4 electrodes, indicating the synergistic effect of using Fe_2O_3 as a support [44]. In the case of C-doped $CoFe_2O_4$ linked to Fe_2O_3, a significantly lower overpotential requirement was noted [45], that is, the C-doped $CoFe_2O_4$/Fe_2O_3 required 260 mV of overpotential to produce an OER current density of 100 mA cm^{-2} and an HER overpotential of 236 mV, indicating excellent catalytic activity for overall water splitting. Similarly, the conjugation of Mo in addition to Co (as an alloy) with Fe_2O_3 has shown promising water-splitting results [46] owing to its bifunctional catalytic properties. The fabrication of a CoMo-Fe_2O_3 heterojunction on a nickel foam involved two sections, in which Fe_2O_3 was first deposited on the nickel foam using the hydrothermal method, followed by CoMo alloy deposition using the electrodeposition technique. The Fe_2O_3 nanostructure on the nickel foam appeared to have a nanosheet morphology, whereas the CoMo alloy showed spherical microparticles distributed evenly on the Fe_2O_3 nanosheets. The unique two-dimensional structure with spherical particles in the CoMo-Fe_2O_3 system could result in increased penetration of electrolyte ions, leading to an increase in the number of reaction sites, and thus, enhanced electrocatalytic activity. The electrochemical characterization results of CoMo-Fe_2O_3 revealed an impressive current density value of 50 mA cm^{-2} for the OER process at the lowest overpotential of 266 mV. On the other hand, the 10 mA cm^{-2} of HER current was recorded at an potential value of 71 mV. The Tafel slope for OER and HER activity was found to be 54 and 85 mV dec^{-1}, respectively. The practicality of the CoMo/Fe_2O_3 catalyst was demonstrated by using two electrode setups for alkaline water splitting that exhibited a current density of 10 mA cm^{-2} at a lower bias voltage of 1.5 V. A theoretical study on CoMo/Fe_2O_3 revealed the formation of an effective interface that facilitated efficient charge redistribution and transfer, leading to enhanced catalytic activity. Importantly, a remarkable stability of over 100 h was recorded under prolonged electrolysis conditions as a bifunctional catalyst. Alothman et al. [47] have proposed the Fe_2O_3@CuO heterojunction as a bifunction catalyst for water electrolysis. Using a simple hydrothermal method followed by calcination, Fe_2O_3@CuO catalysts were synthesized; these were then coated onto a nickel foam by forming an ink with nafion. The optimized Fe_2O_3@CuO electrode exhibited OER and HER overpotentials of 230 and 130 mV, respectively, reaching 10 mA cm^{-2} of current density. Furthermore, a Tafel slope of 54 and 77 mV dec^{-1} was observed in the OER and HER voltammograms, respectively.

Noble metal catalysts could be anchored to Fe_2O_3 to enhance its activity and bifunctionality and reduce costs. For example, Fe_2O_3 and IrO_2 are well known OER catalysts; in contrast, their HER activity is rarely exploited. However, a composite of Fe_2O_3 and IrO_2 was found to perform effectively as a HER catalyst, as demonstrated by Yang et al. [48]. A

thermal decomposition method was used that effectively optimized the IrO_2 and Fe_2O_3 content. The electrochemical measurements conducted in H_2SO_4 (0.5 M) indicated that the adsorption of hydrogen was more efficient on the IrO_2/Fe_2O_3 composite compared to its individual counterparts, resulting in a shift of overpotential onset toward the 0 V vs. RHE, due to the Volmer–Heyrovsky mechanism. Similarly, Mosallaei et al. [49] developed a RuO_2–Fe_2O_3 catalyst using the Ru-ionic complex. The proposed strategy differentiates itself from the reported methods by not using common metal salts for the oxide catalyst synthesis. In this approach, the synthesized Ru and Fe complex $(Ru(then)_3]_2[Fe(CN)_6]$ and $[Ru(phen)_3]$ $[Fe(CN)_5(NO)]$) were calcined to yield the RuO_2–Fe_2O_3 nanocrystal catalyst. A morphological analysis indicated good crystallinity of RuO_2–Fe_2O_3 with an average particle size of 8–12 nm. In the OER and HER experiments, the RuO_2–Fe_2O_3 catalyst exhibited an overpotential value of 292 and −148 mV, respectively, to produce a current density of 10 mA cm^{-2}. The low Tafel slope values of 56.08 and −43 mV dec^{-1} were calculated from the OER and HER process LSV curves, respectively. The low charge transfer resistance at the electrolyte interface indicated the utilization of holes and electrons for OER and HER activity, confirming the superior bi-functional catalytic activity of the RuO_2–Fe_2O_3 catalyst. A similar strategy was employed by Mosallaei et al. [50] to produce a RuO_2–Fe_2O_3 catalyst using metal complexes. In their protocol, an impregnation method was used by utilizing $[Ru(dmbpy)_3]_3[Fe(CN)_6]_2$, an ionic pentanuclear complex, followed by thermal decomposition to yield RuO_2–Fe_2O_3 on a reduced graphene oxide nanosheet support. The nanorod and cubic-shaped RuO_2–Fe_2O_3 were found to be evenly distributed on the reduced graphene oxide nanosheets, indicating the presence of effective diffusion pathways via the superior conductivity and charge transfer properties of the reduced graphene oxide nanosheets during the water splitting reactions. Owing to their superior catalytic and nanostructure properties, the RuO_2–Fe_2O_3 and highly reduced graphene oxide nanosheets deposited on glassy carbon electrode exhibited an OER and HER overpotential value of 386 and −239 mV and a Tafel slope value of 67 and −97 mV dec^{-1}, respectively, in a 1 M KOH electrolyte. Furthermore, significant stability of the catalysts over 16 h was observed during the chronoamperometric measurements. Conclusively, the systematically arranged RuO_2–Fe_2O_3 catalysts on highly reduced graphene oxide nanosheets were shown to offer significantly increased catalytic sites with increased reaction surface area and porosity, leading to a synergistic effect for enhanced overall water splitting.

Yan Sang, ref. [51] proposed a one-step hydrothermal fabrication method for a Fe_2O_3/NiO bifunctional catalyst for water splitting. The material morphology showed a systematic distribution of Fe_2O_3 nanoparticles (50–80 nm) on hexagonal-shaped NiO nanoflakes. The LSV measurements in 1.0 M KOH indicated that Fe_2O_3/NiO required an OER overpotential of 224 mV and a HER overpotential value of 187 mV to achieve 10 mA cm^{-2} of current density. Furthermore, a Tafel slope of 20.0 and 53.8 mV dec^{-1} was observed from the LSV data of the OER and HER activity, respectively. Importantly, Fe_2O_3/NiO demonstrated its bifunctional catalytic activity by exhibiting alkaline overall water splitting at a cell potential value of +1.63 V vs. SHE and over 20 h of stability. The enhanced OER and HER performance of the Fe_2O_3/NiO catalyst was ascribed to the optimized electronic structure of heterojunctions, owing to the optimum level of oxygen vacancies in Fe_2O_3 that favor efficient charge transfer to improve the catalytic activity. The introduction of WO_3 into the Fe_2O_3/NiO catalyst was found to decrease the required overpotential [52]. However, unlike Fe_2O_3/NiO, the WO_3/Fe_2O_3/NiO catalyst functioned as only an OER catalyst, rather than as a bifunctional catalyst. The adopted synthesis method involved simultaneous hydrothermal treatment, comprising an etching reaction and the decomposition of metal ions. Such a synthesis approach caused the regulation of the intrinsic electronic properties of the catalysts due to the presence of high-density heterometal-oxygen bridge sites at the interface. A remarkably low overpotential value of +211 mV was shown to achieve 100 mA cm^{-2} of OER current density. Furthermore, a low Tafel slope of 39.5 mV dec^{-1} indicated excellent catalytic properties, and a stability of over 100 h was observed. A detailed mechanistic study indicated that the presence of W in the

catalysts sped up the oxidation of Ni to the 3+/4+ state from the 2+ state due to the partial electron transformation from the high valence W^{6+} state. Among the reaction intermediates, a weaker adsorption energy of OH* was expected on WO_3 and a stronger one on Fe_2O_3. Being a stronger Lewis acid, W^{6+} readily oxidizes the neighboring Ni^{2+} and Fe^{3+} via the withdrawal of electrons. This mechanism optimizes the adsorption energies of the reaction intermediates and thus enhances the catalytic activity [52]. Conclusively, the presence of W has been revealed to be the key factor in achieving the lower overpotential of OER activity in Fe_2O_3/NiO catalysts. However, in the case of Fe_2O_3/$Ni(OH)_2$ and Fe_2O_3/NiFe alloy nanoparticles, a slightly higher OER overpotential was observed [53,54] indicating that anchoring Fe_2O_3 with NiO and WO_3 offers efficient OER catalysis.

The conjugation of Fe_2O_3 with MnO enhances the OER activity, as reported by Kim et al. [55]. A simple sol-gel technique was proposed to synthesize individual and heterojunctions of MnO and Fe_2O_3. In their electrochemical investigation, the materials were coated onto a Ni foam substrate (as a current collector) in the electrolyte. The electrochemical tests conducted in alkaline media indicated that the MnO–Fe_2O_3 heterojunction reached 10 mA cm^{-2} of current density at a bias potential of +1.60 V vs. SHE; this was ascribed to the overpotential value of +370 mV. Furthermore, a 66 mV dec^{-1} Tafel slope was recorded with a cycle stability of over 1000 cycles. Even though the overall overpotential requirement at 10 mA of current density was not high enough compared to the literature, the heterojunction was found to perform significantly better than its individual counterparts. Notably, the underlying mechanism indicated the synergistic effect of Mn and Fe, which induce the oxidation of O_2 and the reduction of H_2, respectively.

Recently, Fe_2O_3 has been used to oxidize hydrazine in an asymmetric electrochemical cell with a FeP cathode to produce H_2 [56]. In that report, electrolyzed carbon paper was used as a substrate and current collector. The Fe_2O_3 nanostructures were deposited on the substrate (referred to as electro-oxidized carbon paper) via the self-assembly of iron phthalocyanine, followed by pyrolysis in air (Figure 6). For the cathode electrode, the Fe_2O_3 deposited on the substrate was further treated with NaH_2PO_2 in the CVD system for phosphidation, yielding FeP on electro-oxidized (EO) carbon paper (Figure 6). Both the Fe_2O_3 and FeP deposited on the EO carbon paper appeared to show a mosslike morphology, in which the latter showed a weaker surface due to the Kirkendall effect. The morphology appeared to consist of closely packed nanocrystals which provided effective catalytic sites, whereas the porous architecture led to the effective diffusion of electrolyte ions and provided effective gas evolution pathways. In the absence of hydrazine, the OER overpotential was observed at +1.56 V vs. SHE to produce 10 mA cm^{-2}. Both Tafel plots and impedance values showed decreased slope and charge transfer resistance values, respectively indicating the advantages of coupling Fe_2O_3 and FeP in a two-electrode system for hydrazine oxidation for H_2 production. In particular, to reach a hydrazine oxidation current density of 10 mA cm^{-2} at the Fe_2O_3 anode, a potential of 664 mV was required with a Tafel slope value of 179.2 mV dec^{-1} (Figure 7a,b). In contrast, a HER current density of 10 mA cm^{-2} at FeP was achieved with an overpotential of +77 mV with a Tafel slope value of 63.9 mV dec^{-1} (Figure 7c,d). The electrochemical tests conducted in two-electrode setups consisting of a Fe_2O_3 anode and a FeP cathode on electrooxidized (EO) carbon paper indicated an efficient hydrazine oxidation (at the anode) current density of 10 mA cm^{-2} at an impressively lower overpotential of +930 mV, along with the evolution of H_2 gas at the FeP cathode. This study indicated that an alternate reaction for water oxidation with Fe_2O_3 could be beneficial in achieving higher current densities with lower overpotentials. Such systems are believed to represent a key strategy in the fabrication of membrane-less or decoupled electrolysis systems.

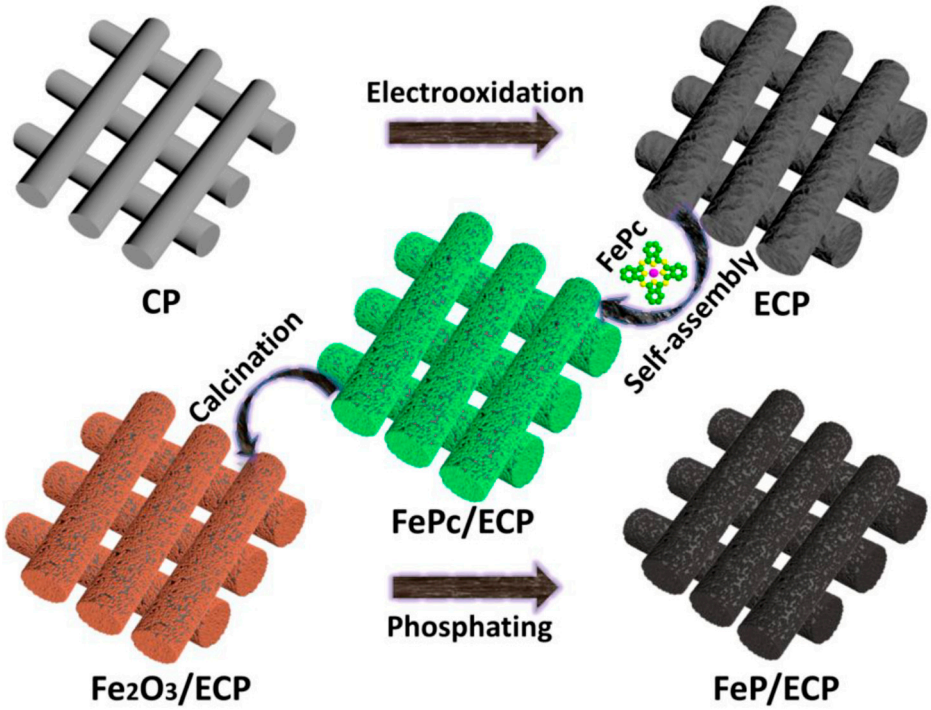


Figure 6. Synthesis protocol of Fe_2O_3 and conversion to FeP on an ECP (electro-oxidized carbon paper) substrate. Adapted with permission from [56]. Copyright [2018] American Chemical Society.

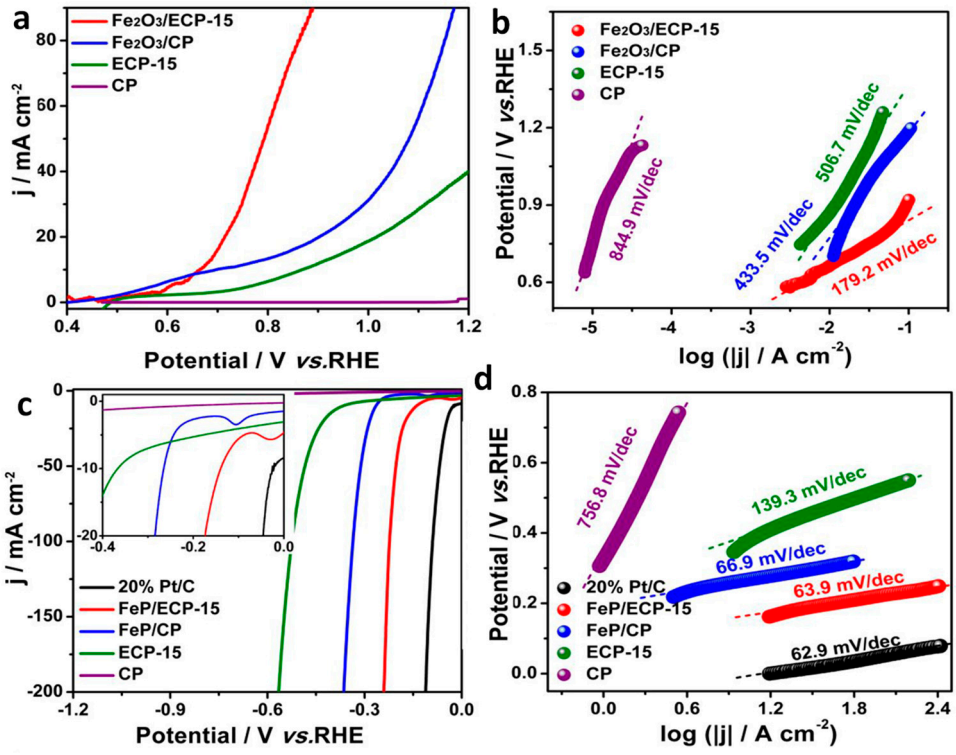


Figure 7. (**a**,**c**) LSV and (**b**,**d**) Tafel plots of Fe_2O_3 and FeP systems on CP and ECP substrates. Adapted with permission from [56]. Copyright [2018] American Chemical Society.

The Fe_2O_3 and FeP heterojunction systems could be synthesized using a hydrothermal method with iron and red phosphorus as precursors [57]. A study of the morphology of the hydrothermally synthesized Fe_2O_3-FeP revealed that FeP consists of a nanorod structure, whereas Fe_2O_3 forms as cubic nanoparticles. The morphology showed the presence of a

porous system that could be utilized for the effective diffusion of electrolyte ions and the removal of the produced gases. The electrochemical experiments conducted in an alkaline electrolyte (1 M KOH) indicated an impressive OER overpotential of +264 mV to achieve 10 mA cm^{-2} of current density. Furthermore, the low value of the Tafel slope and resistance value (at the electrode/electrolyte interface) indicated the excellent catalytic activity offered by the Fe_2O_3/FeP heterojunction. A prolonged water splitting test indicated a stability of over 12 h with two electrode setups, with a potential requirement of only +1.65 V vs. SHE.

Unlike FeP anchored to Fe_2O_3 systems, FeS linked to Fe_2O_3 showed a decreased efficiency, indicating that FeP serves as an effective junction material compared to FeS in terms of OER activity [58]. In contrast, FeS anchored to Fe_2O_3 demonstrated a significantly lower overpotential in the study reported by Guo et al. [59]. In that study [59], the FeS/Fe_2O_3 catalyst (on the iron foam) was fabricated using a semi-sacrificial template approach that involved a solvothermal approach to produce Fe_2O_3, followed by exposure to air and treatment with a sulfide precursor to form FeS. The FeS/Fe_2O_3 showed a nanosheet morphology with an average size of 0.8 μm. A high-resolution TEM analysis confirmed nanojunction formation between the Fe_2O_3 and FeS, with good crystallinity and uniform distribution of elements. The formation of heterojunctions between Fe_2O_3 and FeS offered an effective interface with a tuned electronic structure, leading to effective an electron-proton transfer process that increased the number of active sites with improved stability and OER activity. The optimized FeS/Fe_2O_3 system generated 10 mA cm^{-2} of current density at a lower overpotential value of +266.5 mV. Moreover, enhanced stability of over 50 h was recorded with a Tafel value of 51.17 mV dec^{-1}. The efficient catalytic activity and stability indicated the potential applicability of this material in industrial scale hydrogen production via electrolysis. Similar to iron sulfide, iron selenide anchored to Fe_2O_3 is known to exhibit excellent electrocatalytic water-splitting activity, as demonstrated by Sohail et al. [60]. As such, Fe_2S_3 has been used in OER. However, unlike FeS-Fe_2O_3, Fe_2Se_3/Fe_2O_3 shows a remarkably low overpotential value of +160 mV for OER activity at 20 mA cm^2, implying the lowest applied potential of +1.31 V vs. SHE. Indeed, the overpotential value exhibited by Fe_2Se_3/Fe_2O_3 was found to be the lowest for the Fe_2O_3-based electrode. Furthermore, excellent stability over 24 h was observed during chronoamperometric tests, with a stable current density of 65 mA cm^{-2} at a bias potential of +1.65 V vs. SHE.

4.6. Fe_2O_3 Supported on Carbon Materials

Fe_2O_3 is known for its efficient conductivity compared to other metal oxides. Hence, providing a support material becomes essential for the diffusion/transfer of charges during catalysis. In such cases, the tuning of the catalyst morphology and the conductive nature of the support materials are vital for improved electrocatalytic activity. In the case of Fe_2O_3, limiting its nanomorphology by strategically tuning the crystal size and nanoarchitecture is effective due to its limited carrier path length. Specifically, limiting the nanostructure of Fe_2O_3 to one or two dimensions can boost the catalytic activity by orders of magnitude compared to its microstructures [82]. In addition, providing a highly conductive platform such as graphene (including other carbon supports) to Fe_2O_3 will further support the catalytic activity and stability by effectively and rapidly diffusing the charges that are responsible for catalytic reactions and conductivity [83–85]. For example, anchoring Fe_2O_3 hollow nanorods to carbon nanotubes (CNT) has been found to enhance the OER activity [61]. A Fe_2O_3-CNT junction could be fabricated via the co-precipitation method using urea. Even though the achieved overpotential, Tafel slope, and stability values were +383 mV, 68 mV dec^{-1}, and 12 h, respectively, the values were less significant compared to those in other reports. The strategy of using a carbon support may be a solution to overcome two main challenges, i.e., the limited conductivity of Fe_2O_3 and the poor penetration of the electrolyte on the surface of the catalyst. Furthermore, the introduction of CNT supports the underlying faradaic process by decreasing the resistivity. As a result, the Fe_2O_3-CNT performed better as a catalyst than pristine Fe_2O_3.

Zang et al. [62] investigated the OER activity of Fe_2O_3 anchored to Fe-N-doped carbon nanosheets. A high-temperature facile pyrolysis (1000 °C) approach was proposed to yield mesoporous Fe/Fe_2O_3-Fe-N-doped carbon nanosheets using shrimp shells. The optimized catalyst on GCE exhibited an OER current density of 10 mA cm^{-2} at +0.69 V (vs. Ag/AgCl) and a Tafel slope of 77.5 mV dec^{-1} with a stability of 10 h. Notably, the OER performance of the Fe/Fe_2O_3-Fe-N-doped carbon nanosheets was significant compared to commercial RuO_2. Similarly, Fe_2O_3 deposited on graphitized-carbon nitride nanocomposites was used in OER with alkaline media [63]. The electrochemical results were less significant compared to those of Fe/Fe_2O_3-Fe-N-doped carbon nanosheets. However, Fe_2O_3 anchored to N-doped carbon nanomaterial showed HER activity in alkaline media [64]. That is, unlike other carbon supports on Fe_2O_3, the catalyst, as reported by Jiang et al. [64], showed HER activity. An electrochemical analysis performed in 1 M KOH revealed a HER current density of 10 mA cm^{-2} at an overpotential of +245 mV with a Tafel slope value of 76.6 mV dec^{-1}. Furthermore, excellent stability of the catalyst was observed up to 48 h of water splitting.

The introduction of Ni_3S_2 along with Fe_2O_3 anchored to N-doped carbon composites has been shown to yield excellent OER and HER activities [65]. Even though Ni_3S_2 is well known for its catalytic activity, its lifespan tends to be short due to ineffective coupling to the back contact or substrates. To overcome this challenge, the utilization of Fe_2O_3 and N-doped carbon composite has been proposed. A facile thermal decomposition approach was used with essential precursors to fabricate a Ni_3S_2/Fe_2O_3/N-doped carbon composite. The characterization of the catalyst-deposited nickel foam revealed nanosheets of Ni_3S_2 containing Fe_2O_3 and N-doped carbon particles. An electrochemical analysis conducted in 1 M KOH indicated that the Ni_3S_2/Fe_2O_3/N-doped carbon composite exhibited an impressive OER overpotential of 188 mV for 52 mA cm^{-2} of current density, along with a Tafel slope value of 64.3 mV dec-1. In addition, about 10 mA cm^{-2} of HER current density was produced at an overpotential value of +74 mV with a Tafel slope of 115.8 mV dec^{-1}. Importantly, the electrode composite in the bifunctional mode in two electrode systems was found to achieve about 100 mA cm^{-2} of current density at a bias potential of +1.605 V vs. SHE, which was supplied using an external battery. The superior catalytic activity achieved in this report indicates that the utilized synthesis approach and the composite anchored to Ni_3S_2 result in a strong coupling of the catalyst to the nickel foam substrate.

The simultaneous deposition of Fe_2O_3 and graphene oxide on a nickel foam substrate can be achieved using the co-deposition method [66]. The approach involves separate graphene oxide and Fe_2O_3 (sugar-cubic) synthesis using a modified Hummers method and hydrothermal method, respectively, followed by electrodeposition to deposit the materials on the Ni foam. An electrocatalytic characterization conducted in 1 M KOH showed an overpotential value of +313 mV to generate an OER current density of 100 mA cm^{-2}; this was ascribed to the Tafel slope of 81 mV dec^{-1}. The improved OER overpotential value of Fe_2O_3/graphene oxide was ascribed to the increased surface area of the nitrogen-doped graphene with effective mechanical properties that provide stability and enhanced active sites during electrolysis. Furthermore, the presence of uniformly distributed Fe_2O_3 nanocrystals on nitrogen-doped graphene offered increased reaction sites, favoring an effective interface at the electrolyte and providing a solid foundation for charge collection and diffusion/transfer. Likewise, dispersing Fe_2O_3 on MWCNT could also provide similar advantages to graphene in terms of increasing the OER activity of Fe_2O_3 [67]. In other words, the presence of MWCNT as a support for Fe_2O_3 favors the adsorption of OER intermediates that drive efficient charge transfer kinetics. Surface-functionalized multiwall carbon nanotubes act as an effective support to the uniform deposition of Fe_2O_3, which was achieved by pulsed laser ablation deposition. The LSV measurements were noted to produce 10 mA cm^{-2} of current density at a lower overpotential of +310 mV and a Tafel slope of 20.35 mV dec^{-1}, confirming the superior OER activity of Fe_2O_3/MWCNT compared to its counterparts. The presence of MWCNT decreased the energy barriers of the OER intermediates, which are rate-determining. However, a limited stability of only 10 h was observed, which may not be significant compared to other electrode combinations that

support Fe_2O_3. Therefore, among the tested carbon supports for Fe_2O_3, Ni_3S_2 anchored to N-doped carbon composites was found to yield superior OER activity, in addition to HER activity.

4.7. Fe_2O_3 Linked to MOFs

Recently, MOFs have gained significant attention in energy applications owing to their unique architecture, i.e., containing organic ligands linked to metal clusters [86]. MOF offers tunable porosity with an enhanced specific surface area that could be engineered into specific morphologies depending on the application needs. Using the unique properties of Fe_2O_3, Niu et al. [68] proposed FeOx node-based MOFs with engineered intrinsic active sites and architectures with enhanced reaction areas that exhibited excellent OER, HER, and ORR activities. The procedure involves the simple solvothermal method that allows extensive tuning of bonding between the Fe and 1,4-dicarboxybenzene ligands to be undertaken via the utilization of different solvent systems and a wide range of metal sources. Such tuning provides effective control over the selective or desired morphologies, such as concave octahedral, rod-like, spindle-like, and octahedron-like, offering desirable properties (Figure 8).

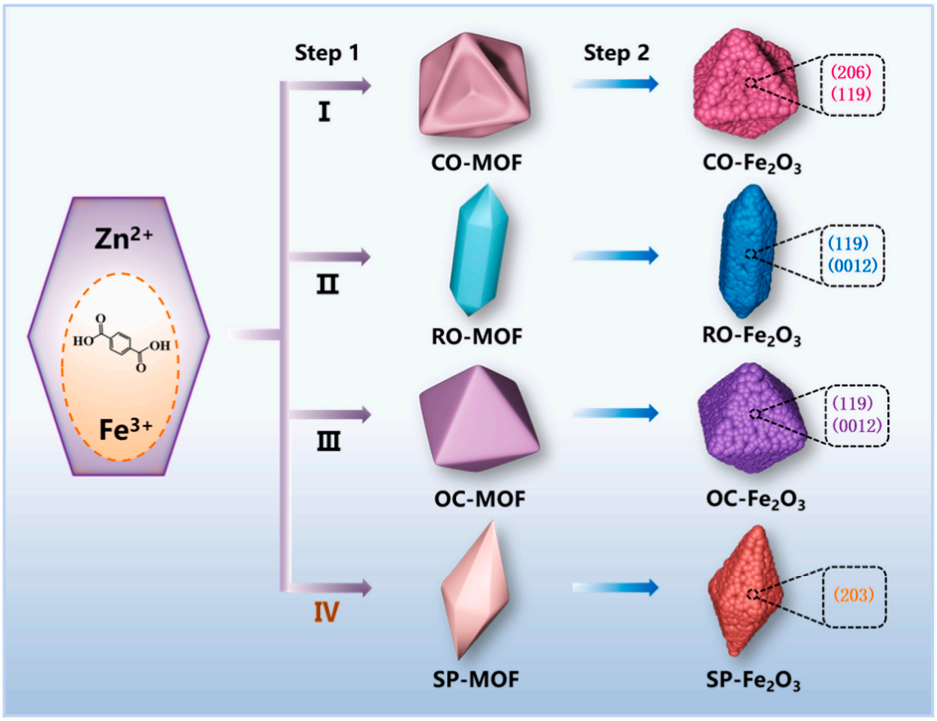


Figure 8. Synthesis of morphologically tuned Fe_2O_3 from MOF. CO—a concave octahedral structure, RO—a nanorod-like structure, OC—octahedron, SP—a spindle structure. Reused with permission from [68]. Copyright 2021, with permission from Elsevier.

Furthermore, a pyrolysis step was proposed to yield a graphite nanocomposite of Fe_2O_3 that displayed a wide range of exposed crystal planes having unique properties and reaction capabilities with retained original morphologies (Figure 8). Figure 9 shows the LSV, Tafel slope, and I-t stability plots of concave octahedral, rod-like, spindle-like, and octahedron-like MOF-Fe_2O_3 for OER and HER applications. Among the explored structures, the concave octahedral form of Fe_2O_3—MOF was found to possess an enhanced active site, owing to the favorable facets for improved electrocatalytic OER and HER activity, with enhanced stabilities, as shown in Figure 9 [68]. Importantly, the results of this report indicate the applicability of Fe_2O_3 in MOF systems in terms of electrocatalytic activity.

4.8. Sea/Domestic Wastewater Electrolysis

Sources of freshwater around the globe are valuable and limited, and thus, the utilization of seawater and domestic sewage in electrolysis is encouraged on the basis of cost efficiency and resource availability. However, the electrochemical water splitting of seawater is challenging due to the presence of unwanted and interfering ions, decreased conductivity, poisoning, and corrosion of the electrodes/catalysts [87,88]. The presence of chloride anions leads to the evolution of chlorine in the OER process that causes corrosion, poisons the anodic surface through the formation of insoluble precipitates, and compromises efficiency [89]. To inhibit the evolution of chlorine and selectively perform OER, a systematically designed catalyst needs to be implemented. Li et al. [69] proposed seawater and domestic sewage water electrolysis using a Fe_2O_3/NiO interface. A simple chemical bath deposition method was proposed for the synthesis of Fe_2O_3 on Ni foam-producing porous structures. The characterization of the catalyst indicated the formation of a FeNi oxide interface that exhibited superior OER activity. In a 0.1 M KOH electrolyte, the Fe_2O_3/NiO exhibited a 10 mA cm^{-2} current density at an overpotential value of +182 mV but also a high current density of 1000 mA cm^{-2} at an overpotential of +267 mV. Both the Tafel slopes and EIS measurements indicated low slope and charge transfer resistance values, respectively. An impressive stability of over 50 h was recorded in both seawater and domestic sewage water, indicating the versatility of the Fe_2O_3/NiO catalyst. The superiority of Fe_2O_3/NiO was further tested in two electrode setups using seawater and alkaline domestic sewage. For this, a $NiMo_4/MoO_2$ electrode was used as a cathode and compared with Pt/C in terms of practicality. With alkaline electrolytes including NaCl and sea water-containing mixtures, the Fe_2O_3/NiO catalyst performed significantly better compared to commercial RuO_2 OER and Pt/C HER electrode systems, indicating exceptional selectivity of Fe_2O_3/NiO in the OER process. Furthermore, a stability of over 50 h was observed, indicating no apparent corrosion of the electrodes in Cl^- containing electrolytes. Similarly, the potential application of Fe_2O_3/NiO was tested in alkaline sewage electrolysis, as demonstrated in Figure 10. Interestingly, to perform OER with 100 mA cm^{-2} in alkaline sewage system, the Fe_2O_3/NiO utilized an overpotential of +222 mV, which was observed to be lower than that of the standard RuO_2 OER catalyst, both in three- and two-electrode setups (Figure 10a,b). With an elevated current density of 500 mA cm^{-2}, the bias potential was noted to be +1.752 V vs. SHE, which confirmed the pilot scale industrial feasibility of the Fe_2O_3/NiO catalyst. Mainly the catalyst performance was found to be consistent, despite the high chemical oxygen demand; this confirmed the anti-poisoning characteristic of Fe_2O_3/NiO as a catalyst. A photographic image of a Fe_2O_3/NiO anode catalyst connected to standard battery with a $NiMo_4/MoO_2$ cathode catalyst is shown in Figure 10, confirming the formation of gas bubbles. The I-t plot shown in Figure 10d further confirms the stability of Fe_2O_3/NiO for more than 30 h of operation, indicating the catalytic performance and selectivity of the catalyst.

Cui et al. [71] proposed an effective and cost-effective method for the synthesis of a Ru, Ni-doped Fe_2O_3 bifunctional catalyst for alkaline and seawater splitting. The synthesis protocol involves the use of precursors in autoclave and hydrothermal synthesis with systematic optimization regarding the ratio of Ni and Ru. The optimized Fe_2O_3 bifunctional catalyst exhibited 100 mA of OER and HER current density at an overpotential value of +329 and +75 mV, respectively, in a 1.0 M KOH electrolyte. In a two-electrode setup as the bifunctional electrode mode, the RuNi-Fe_2O_3 required a very low applied potential of +1.66 V vs. SHE in the standard alkaline electrolyte. Importantly, in the seawater electrolyte, a significantly low overpotential of +1.73 V vs. SHE was optimized, indicating the effectiveness of the catalyst in practical applications. The selectivity and stability were further proved by testing the RuNi-Fe_2O_3 for long-term seawater electrolysis, as shown in Figure 10e. The I-t plot (Figure 10e) suggests excellent stability over 100 h of seawater splitting, indicating the superior performance of RuNi-Fe_2O_3 as a bifunctional catalyst. The standalone device shown in Figure 10f shows a two-electrode setup with a RuNi-Fe_2O_3 bifunctional catalyst for seawater splitting. Furthermore, using commercial solar panels,

the electrode system was utilized to perform seawater electrolysis using a RuNi-Fe_2O_3 bifunctional catalyst. The efficacy was compared with that of a standard RuO_2-Pt/C electrode system, as shown in Figure 10f. The rapid evolution of gas bubbles, along with the increase in balloon volume, confirmed that the proposed catalytic system could be effectively employed in seawater electrolysis and could replace the PGM electrodes in alkaline water electrolysis systems.

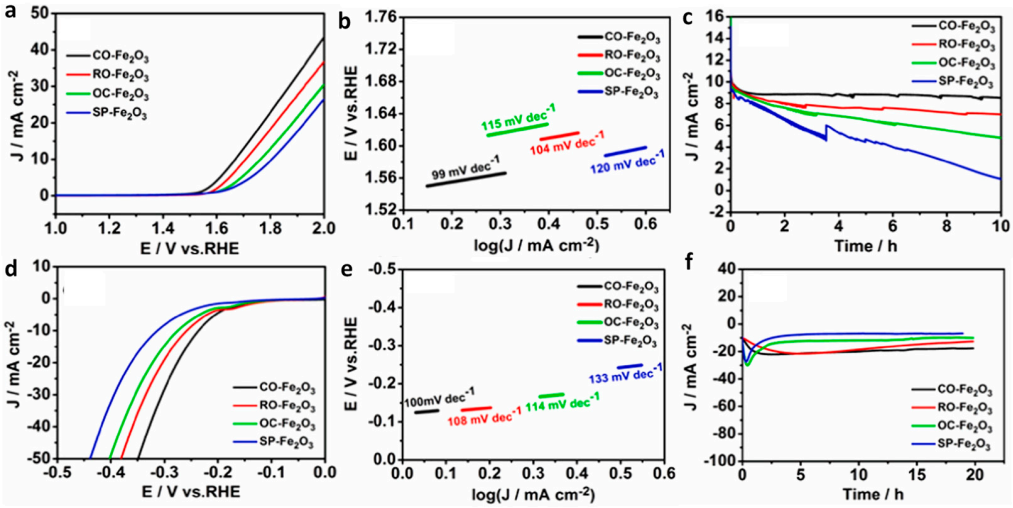


Figure 9. (**a**,**d**) LSV curves (**b**,**e**) Tafel plots and, (**c**,**f**) I-t plots for morphologically tuned Fe_2O_3 in terms of OER and HER activity. Reused with permission from [68]. Copyright 2021, with permission from Elsevier.

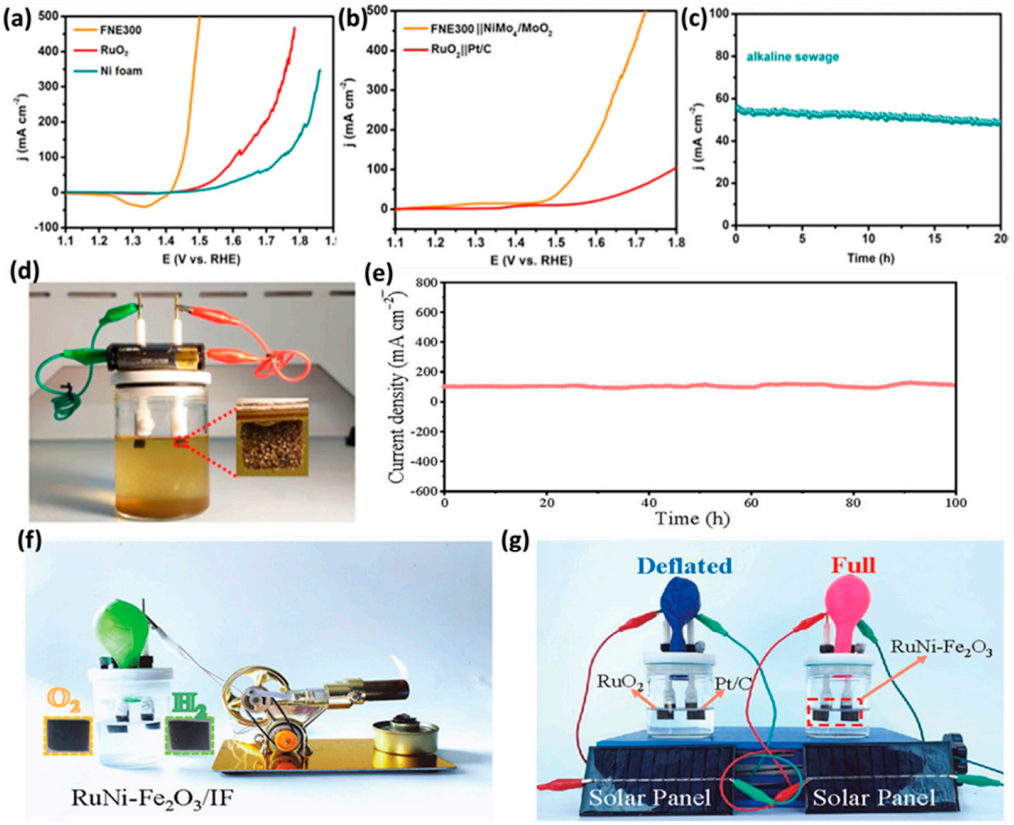


Figure 10. (**a**) LSV curves of the FNE300 (FNE300 represents Fe_2O_3/NiO heterojunction system) compared to the standard RuO_2 and Ni foam substrate, measured using an alkaline sewage electrolyte.

(**b**) LSV curves standard RuO_2||Pt/C and FNE300||$NiMo_4/MoO_2$ in standard electrolyzers system measured using an alkaline sewage electrolyte. The (**c**) I-t plot (**d**) photographic image of FNE300||$NiMo_4/MoO_2$ system in electrolysis condition. Adapted with permission from [69]. Copyright [2021] American Chemical Society. (**e**) I-t plot of RuNi-Fe_2O_3 measured in alkaline seawater showing incredible stability. (**f**) The two-electrode setup for seawater electrolysis. (**g**) A comparison of the electrolysis activity of RuNi-Fe_2O_3 with a standard RuO_2||Pt/C system powered using commercial solar panels. Reused with permission from [71]. Copyright [2022], with permission from Elsevier.

P-doped Fe_2O_3 decorated on CoP could be utilized to split seawater into H_2 and O_2, as demonstrated by Cui et al. [70]. Specifically, P-Fe_2O_3 was utilized to overcome the poor H–OH moiety dissociation on CoP, as well asl the inefficient desorption of intermediate molecules. Nanosheets of P-Fe_2O_3-CoP were fabricated using two two-step processes involving hydrothermal and gas-phase phosphorization procedures. During the water splitting process, the presence of P as a dopant was found to fulfill two main purposes, i.e., the introduction of an essential interfacial structure and defects. The optimized catalyst exhibited superior catalytic activity compared to the standard RuO_2 catalyst. In seawater and freshwater electrolytes (containing 1 M KOH), a significantly low overpotential of +270 and +250 mV to generate 10 mA cm^{-2} of current density was observed. Furthermore, when employed as a bifunctional catalyst in a two-electrode electrolysis assembly, the P-Fe_2O_3-CoP catalyst exhibited a required bias potential of +1.61 vs. SHE for fresh water and about +1.65 V vs. SHE for seawater splitting reactions (for 10 mA cm^{-2}). The low Tafel slope values, decreased electrode/electrolyte charge transfer resistance, and prolonged stability further confirmed the efficacy of the P-Fe_2O_3-CoP catalyst in fresh water and seawater electrolysis.

4.9. Influence of Magnetic Fields on Catalysts

The utilization of magnetic fields during electrolysis is known to provide a significant catalysis effect by accelerating the OER and HER activities [90–92]. The application of magnetic fields during electrolysis could exert different effects on electrolysis systems, improving the efficiency by providing the electrocatalytic effect, magnetohydrodynamic influence, magnetothermal effect, bubble management, magnetic moment alignment, spin selective effect [93,94], etc. Specifically, the formation of gas bubbles at the electrode surface during electrolysis causes decreased efficiency. In the electrolysis industry, an estimated energy loss of ~40% is expected due to the accumulation and inefficient removal of bubbles from the electrode surface [95]. The ineffective removal of gas bubbles may block the electrode surface, causing increased ohmic resistance and inhibiting facile mass transfer and nucleation [96].

Recently, Li et al. [97] demonstrated an effective route of harnessing magnetic fields in catalytic materials to enhance the OER process. This was successfully achieved by employing γ-Fe_2O_3 electrodes, owing to their magnetic properties. Specifically, cubic spinel structured γ-Fe_2O_3 (maghemite) is widely known for its strong magnetic properties and is widely employed as a permanent magnetic material [98]. The authors proposed a super-hydrophilic γ-Fe_2O_3 hydrosol with tuned surface wettability and magnetism for application under magnetic fields. This was achieved by coating the γ-Fe_2O_3 hydrosol on different substrates having unique magnetic and surface properties, such as carbon cloth (CCloth), nickel foam (NF), heat-treated carbon cloth (CCloth-Treated), and carbon paper, using a simple dip-coating method. Figure 11 shows the different setups used to induce magnetic fields in Fe_2O_3 electrodes. For instance, the catalytic activity of super-hydrophilic γ-Fe_2O_3 on NF was confirmed by LSV, Tafel plot, and EIS measurements, as shown in Figure 12a–c, respectively. The γ-Fe_2O_3 exhibited a cathodic shift in the onset potential in the LSV and required only +1.6 V vs. SHE to achieve 50 mA cm^{-2} of current density, whereas only Ni foam required a significant higher potential of +1.73 V vs. SHE to achieve the same result. The cathodic shift in potential confirmed that the presence

of super-hydrophilic γ-Fe_2O_3 favored OER activity over bare Ni foam. Furthermore, the super-hydrophilic γ-Fe_2O_3 showed a decreased Tafel slope (Figure 12b) and polarization resistance (Figure 12c) compared to the untreated Ni foam. In addition, an 80° contact angle was observed for bare Ni foam (inset of Figure 12d), whereas the γ-Fe_2O_3 showed a super-hydrophilic characteristic (inset of Figure 12e). Conclusively, the surface super-hydrophilic property of γ-Fe_2O_3 ensures the effective release of O_2 bubbles at the surface, along with the efficient and rapid transport of the electrolyte toward the electrode surface, leading to improved OER activity.

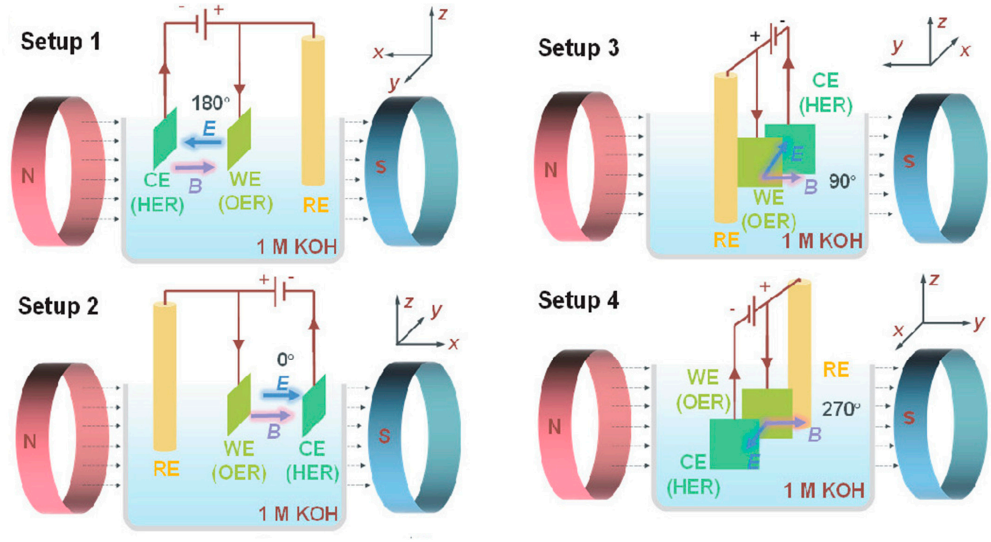


Figure 11. The different experimental setups tested for the application of magnetic fields to an electrode system. Reused with permission from [97]. Copyright 2023, with permission from Elsevier.

The chronoamperometric measurements performed (γ-Fe_2O_3/Ni-foam) in the presence of a magnetic field showed impressive results, indicating the importance and advantages of the use of magnetic fields. Four different setups were tested based on the magnet field input direction and system configuration, as shown in Figure 12. The experimental results confirmed that irrespective of the setup, a significant increase in current density was observed under the influence of a magnetic field. Among the setups, the second system showed a comparatively more significant influence of magnetic fields on OER activity. In the case of diamagnetic substrates, negative results were obtained. Importantly, the use of magnetic fields in electrocatalytic systems was found to provide an added Lorentz and Kelvin force for the effective removal of O_2 bubbles with efficient transport of electrolytes based on the implemented setup and substrates [97].

4.10. Fe_2O_3 in AEMWE Systems

AEMWE has emerged as one of the promising technologies that balances the advantages of both AWE and PEMWE into a single system. AEMWEs are operated in moderately weak alkaline conditions compared to AWE and integrated into membrane-based electrolyzer configurations like PEMWE. Unlike PEMWE, AEMWE may be used in non-PGM-based catalysts without any requirement for acidic electrolytes. Hence, the catalysts integrated into AEMWE are crucial for efficiency and stability. In AEMWE, the cracking of catalysts was found to be one of the limitations that hinders long-term activity and stability. Recently, Chen et al. [72] indicated the importance of Fe_2O_3 (with Co) as an island-type hybrid catalyst in AEMWE electrolysis that significantly inhibits the cracking of the catalysts. Using a systematically developed microwave-assisted hydrothermal technique, an island-type hybrid catalyst containing a controlled ratio of Fe_2O_3 and Co was synthesized. In the AEMWE system, the optimized Fe_2O_3/Co was used as an anode catalyst, whereas Pt/C was used as a cathode catalyst, which was loaded onto a carbon

cloth support using a hand painting technique. The commercially available Fumapem FAA-3 membrane (Fumatech, Bietigheim-Bissingen, Germany) was used in the membrane electrode assembly (MEA) stack. The characterization results showed that the Fe_2O_3 acted as a support on the Co catalyst, providing a nanoscale gap for the effective removal of product gases with the electrolyte fill-ups. The efficiency of the catalyst was found to be dependent on the ratio of Fe_2O_3 and Co, as shown in the LSV and Tafel plots (Figure 13a,b). Electrolysis testing carried out in 1 M KOH (Co-Fe_2O_3 of 60:30 ratio) produced an impressive current density of 200 mA cm^{-2}, which was found to be much higher than the catalyst without the Fe_2O_3 support layer. Stability studies conducted over a longer electrolysis period indicated an impressive stability over 200 h (Figure 13c), with a retention of over 90% of the initial current density. Moreover, the LSV plots measured before and after the stability tests indicated no significant difference, indicating the superior stability of the Co-Fe_2O_3 catalyst (Figure 13d).

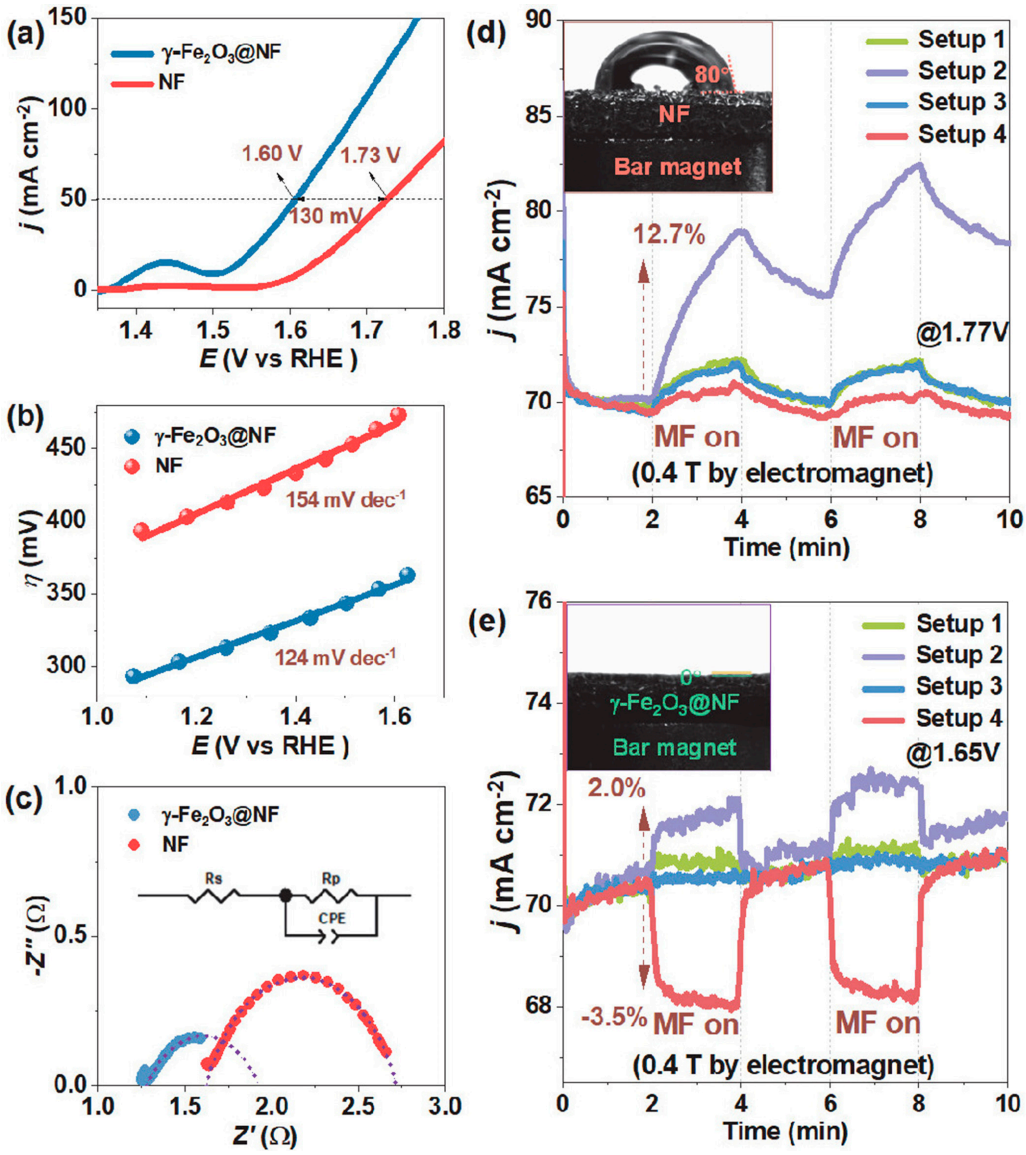


Figure 12. (**a**) LSV, (**b**) Tafel plot, and (**c**) Nyquist plots of γ-Fe_2O_3 (measured at a bias voltage of 1.6 V) on nickel foam for OER, measured in 1 M KOH at a scan rate of 5 mV s^{-1}. Chronoamperometric curves of γ-Fe_2O_3 coated nickel foam measured at a bias potential of (**d**) 1.77 and (**e**) 1.65 V, and inset photographic image showing the respective contact angles under the applied 0.4 T magnetic field. Reused with permission from [97]. Copyright 2023, with permission from Elsevier.

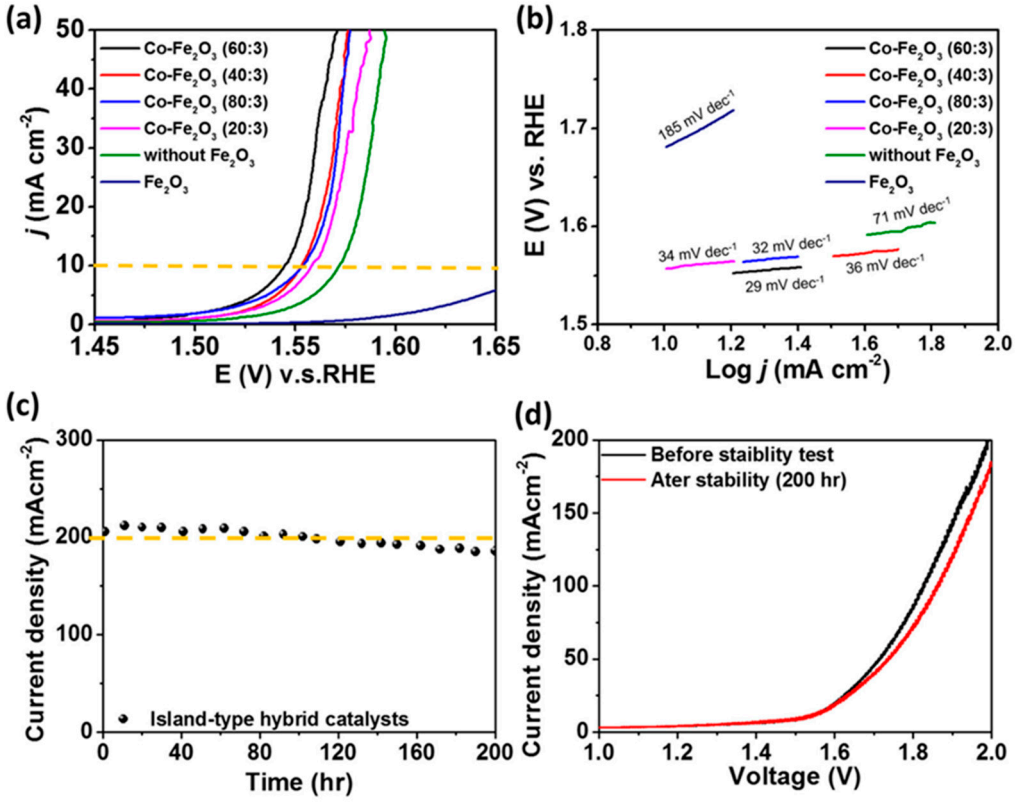


Figure 13. (**a**) Voltammograms and (**b**) Tafel slopes of Co-Fe_2O_3 catalyst with different ratios. (**c**) The stability I-t plot of Co-Fe_2O_3 of 60:30 ratio with (**d**) LSV plot measured before and after the stability tests. Reproduced with permission from [91].

4.11. Fe_2O_3 Supported Ceramics in SOEC

The solid-state structure of SOEC systems offers significant advantages over other hydrogen electrolyzer technologies, e.g., a unique ion diffusion mechanism, high electrode reactivity hydrogen purity, simplistic design, and possible commercial applicability [92]. The solid ceramic electrolyte in SOEC systems that separates the anode from the cathode compartments and provides effective diffusion pathways to O^{2-} ions is one of the important components that determines the overall efficiency and device stability. A wide range of ceramic electrolytes have been proposed in the last few years. Among the electrolytes, yttria-stabilized zirconia (YSZ) has been widely employed, owing to its low conductivity for electrons. In SOEC systems, the oxygen/cathode electrode materials play an important role and are generally doped with Sr for efficient oxygen ion transport and overall cell performance. The use of strontium-doped materials often aligns well with the other components of the SOEC, such as YSZ electrolytes, as evidenced in recent publications. However, during SOEC cell operation, the Sr ions are prone to diffuse and combine with the YSZ material (Zr) to yield $SrZrO_3$. The $SrZrO_3$ formed in the electrolyte is known to be an insulating phase, and its presence restricts the diffusion of oxygen ions through the solid electrolyte toward the cathode electrode. The significant hindrance to the diffusion of oxygen ions has been found to increase the polarization resistance, which influences the SOEC efficiency and device performance. Hence, to inhibit the formation of an insulating $SrZrO_3$ phase in SOEC electrolytes, an interlayer was introduced containing ceria between the Sr-oxygen/cathode electrode and YSZ electrolyte [93,94]. Conclusively, the interlayers play a crucial role in SOEC systems in terms of preventing Sr diffusion, and, at the same time, provide effective pathways for oxygen ion transportation [93,94].

Considering the importance of the interlayer, its properties are known to play a significant role in SOEC performance. For example, a material offering an increased density of oxygen ion conduction is an ideal option for increased performance. Recently, the utilization

of oxides of transition metals has been shown to improve SOEC performance by acting as a grain boundary cleaning agent and a sintering aid for ceramic electrolytes [95–97]. Recently, Qu et al. [98] demonstrated the integration of Fe_2O_3 to a samarium-doped ceria (SDC) interlayer in a SOEC system to improve the ionic conductivity of the cathode electrode. Pristine and Fe_2O_3 doped SDC were synthesized using a glycine-nitrate method, whereas the YSZ electrolyte and $(La_{0.6}Sr_{0.4})_{0.95}Co_{0.2}Fe_{0.8}O_{3-\delta}$ (LSCF) were commercially acquired; the latter was used as the oxygen electrode. For the hydrogen electrode, a glycine-nitrate method was used to obtain NiO. The doped and undoped SDC were prepared by pressing the relevant powders into green sheets (1250 °C for 4 h at a pressure of 10 MPa). During symmetrical cell testing conducted at 800 °C, a significant advantage of Fe_2O_3 doping was observed in terms of oxygen electrode polarization resistance and electrolysis current. The electrolysis current measured at 1.5 V during the symmetrical cell testing revealed a current density of 0.3 A cm^{-2} for the undoped system, which was found to be increased to 0.5 A following Fe_2O_3 doping. On the other hand, the oxygen electrode polarization resistance of undoped systems was noted to be 0.22 Ω cm^{-2}, showing a significant decrease to 0.09 Ω cm^{-2} in the presence of the Fe_2O_3 dopant. Importantly, the introduction of a Fe_2O_3 interlayer dopant led to improved ionic conductivity, cathode electrode stability, and hydrogen production (calculated to be 132 mL cm^{-2} h^{-1} when undoped vs. 195 mL cm^{-2} h^{-1} when doped), which, in turn, boosted the efficiency of SOEC.

5. Potential Application in Commercial Electrolyzers

The commercial applicability of the catalyst in large-scale electrolysis is the most important aspect of the hydrogen electrolysis industry. Being a cheap, stable, and abundant material, Fe_2O_3 could be a potential candidate as a catalyst for the electrolysis industry in the future. In recent research, the applicability of Fe_2O_3 has been successfully tested in AWE, AEMWE, and SOEC systems. Specifically, in basic electrolytes and high-temperature ceramic systems, Fe_2O_3 showed significant stability. However, its poor stability in low pH conditions restricts its use in PEM-based electrolyzers. Owing to its intrinsic and extrinsic characteristics, Fe_2O_3 is mainly used in OER applications and bifunctional systems. Its utilization as solely a HER catalyst has not been widely studied. As discussed above, the direct utilization of Fe_2O_3 in pristine form has limited applicability. However, suitable modifications and/or coupling and alloying with other materials have extended its applicability, efficiency, and stability. Based on this strategy, a wide range of catalytic systems have been proposed and tested. However, studies are limited to three- and two-electrode systems in lab-scale applications. This indicates that the testing of Fe_2O_3 in electrolyzer test systems is lacking, and significant effort is essential in this direction to promote Fe_2O_3 as a catalyst for pilot scale systems in the future. Therefore, studies directed toward the testing of Fe_2O_3-based catalysts in electrolyzer stacks are encouraged. Recent research and advancements have indicated that Fe_2O_3 could be an ideal catalyst material for the AWE, AEM, and SOEC-based electrolyzers of the future. However, the intrinsic and extrinsic characteristics of Fe_2O_3 are mainly exploited in OER applications and bifunctional systems following strategic modifications. Hence, significant research and development of modification strategies of Fe_2O_3 are essential. As presented in the discussion section, the current stages of different modifications indicate improved efficiency, selectivity, and stability of Fe_2O_3-based electrodes in terms of OER activity. In comparison with other metal oxides/hydroxides/alloy-based electrodes, the research focus on Fe_2O_3 has been limited. Hence, the coming years could provide significant milestones in Fe_2O_3-based OER catalysts in electrolyzer systems if suitable modification strategies are employed.

Based on the aforementioned discussion, we provided a brief roadmap of the use of Fe_2O_3 in water electrolyzers, as shown Figure 14a. The primary step involves the synthesis of Fe_2O_3. The synthesis protocol has to be simple and scalable industrial scale production. The next step involves the essential modifications, because the adaptation of suitable modification dictates the efficiency and stability of the catalyst. In this step, the catalyst could be modified to suit bifunctional catalysis, in addition to offering OER

activity. The modification protocols need to be designed carefully to meet the scalable parameters without compromising efficiency, stability, safety, or toxicity. After the essential modifications, testing needs to be performed to assess the efficiency, stability, and necessary conditions on a lab scale. The testing step mostly determines the important parameters and conditions with which the catalyst could be utilized more efficiently. The final step involves the implementation and testing of the catalyst system in AWE, AEMWE, SOEC, and seawater electrolysis stacks to determine its potential applicability.

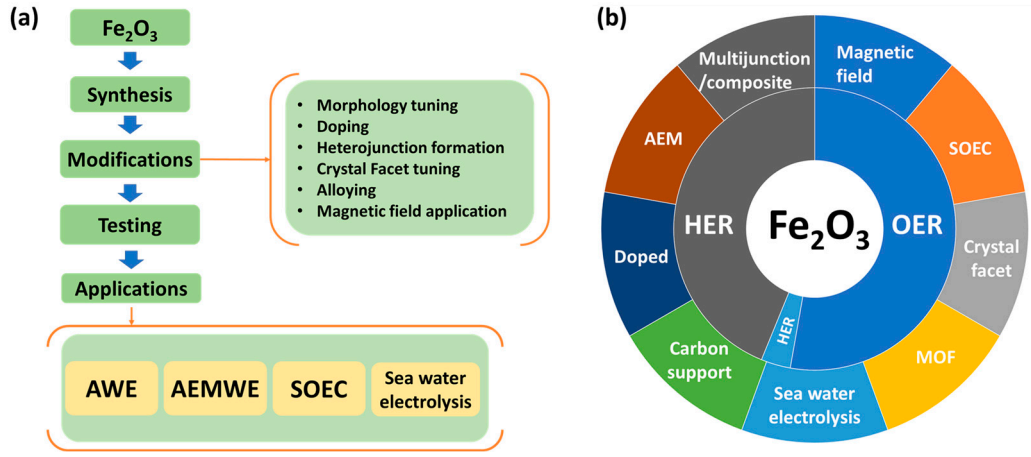


Figure 14. (**a**) Brief roadmap for future works on Fe_2O_3-based catalysts in electrolyzers. (**b**) Sunburst chart of Fe_2O_3 in different catalytic modes (First circle) for OER, HER, and bifunctional applications. The second circle demonstrates the different catalyst systems of Fe_2O_3 applications.

6. Discussion

Figure 14b summarizes the applications and modes of implementation of Fe_2O_3 in electrocatalytic water splitting systems. The low cost of Fe_2O_3, as well as its abundance, geographical availability, and non-toxicity, are the main aspects that drive interest in it as a catalyst in energy applications. Fe_2O_3 is widely employed as an OER (in addition to ORR) catalyst and as a bifunctional catalyst when combined with suitable materials or following modifications. On the other hand, its stand-alone application to HER is limited due to its poor catalysis in water reduction. Overall, the intrinsic and surface properties of Fe_2O_3 allow its effective implementation in water oxidation rather than water reductions. Despite widely reported OER applications, Fe_2O_3 still requires essential modifications to boost its OER activity and stability. As shown in Figure 14b, several strategies have been proposed to boost the OER activity and to implement it as a bifunctional/HER catalyst, as discussed below.

Crystal facet tuning and morphology: Specific facets and certain morphologies are known to offer significantly superior catalytic activities in Fe_2O_3 when compared to other facets and morphologies. Therefore, tuning the morphology to maximize the favorable facets via a controlled synthesis process is vital for enhanced catalytic activity, which would provide efficient charge diffusion. Research on F_2O_3 in this direction is limited, and thus more efforts should be made on designing synthesis schemes to obtain facets with specific morphologies.

Doping: The intrinsic characteristics of Fe_2O_3 are not suitable for its widespread application in, for example, water-splitting reactions. In such cases, doping could emerge as a solution to increase the abundance of catalytic sites via defects or oxygen vacancies and the density of states, which modifies the intrinsic properties of Fe_2O_3 to a certain extent. Even though few attempts have been reported until now, exploring a wider range of dopants could provide new insights into the properties of Fe_2O_3, potentially expanding its water-splitting applications.

Multijunction systems (anchoring to other materials): Anchoring Fe_2O_3 to different oxides, sulfides, phosphides, etc. has been undertaken extensively owing to its multiple

benefits. For example, anchoring PGM catalysts to Fe_2O_3 could limit the excessive utilization of PGM without compromising the catalytic extent. In such cases, Fe_2O_3 acts as an effective platform for catalytic reaction sites. Furthermore, the presence of different metal ions (in a heterojunction system) near the Fe atoms at the surface could influence the adsorption energy and reaction intermediates which ultimately favor electrocatalytic reactions with rapid reactivity and selectivity. Alternatively, exploring other reactions for water oxidation with Fe_2O_3 could be beneficial in terms of achieving higher current densities with lower overpotentials. Such systems are believed to represent a key strategy in fabricating membrane-less or decoupled electrolysis systems. Moreover, heterojunctions having an effective interface with a tuned electronic structure are beneficial for the electron/hole transfer process.

Carbon material supports: The limited charge conductivity of Fe_2O_3 could be overcome by providing a support material for improved electrocatalytic activity. Specifically, limiting the nanostructure of Fe_2O_3 to one or two dimensions and providing a highly conductive platform such as graphene (including other carbon supports) could boost the catalytic activity. Carbon-supported Fe_2O_3 not only overcomes the limited conductivity but also improves the penetration of the electrolyte, increases back contact, increases the number of reaction sites, expands the effective interface, and provides a solid foundation for charge collection and diffusion/transfer.

Fe_2O_3-MOF: By utilizing a controlled and systematic synthesis (precursors) approach, a wide range of Fe_2O_3-MOFs have been obtained, offering tunable porosity and morphology and increased active surface area, resulting in excellent OER and HER activities. However, very limited literature in this direction limits our understanding, and thus, more mechanistic insights are needed.

Seawater electrolysis: Seawater electrolysis is an ambitious target in electrolysis, as sources of freshwater are limited and are essential to human needs; thus, the utilization of seawater and domestic sewage water is encouraged. Such an implementation could also offer benefits in terms of cost, efficiency, and availability. Fe_2O_3 has shown a certain degree of water-splitting activity with significant stability and selectivity in some studies. Specifically, the Fe_2O_3 has been shown to withstand unwanted and interfering ions, which otherwise decrease conductivity and negatively affect the catalytic properties. In some experiments, Fe_2O_3 (anchored system) performed significantly better than commercial RuO_2 OER and Pt/C HER catalysts, indicating exceptional selectivity, stability, and efficiency in seawater electrolysis. A more detailed mechanistic study in this direction could potentially provide insights into Fe_2O_3 charge dynamics which, in turn, would benefit the development of highly efficient catalysts for seawater splitting in the future.

Fe_2O_3 under an applied magnetic field: Magnetic fields applied during electrolysis improve the catalysis by accelerating the OER and HER activities. Specifically, a magnetic field applied to γ-Fe_2O_3 alters the surface super-hydrophilic property that ensures the release of O_2 bubbles at the surface, along with efficient penetration of electrolyte. Additionally, the magnetic field provides an added Lorentz and Kelvin force for the removal of O_2 bubbles that ultimately results in improved water-splitting activity.

Fe_2O_3 in AEMWE: The cracking of catalysts in AEMWE affect their long-term activity and stability. This problem could be solved by using Fe_2O_3 (with Co) catalyst that inhibit cracking. Hence, Fe_2O_3 may play a crucial role in AEMWE in membrane-based electrolyzers in the future. Significant research in this direction is essential, as it could benefit fabrication of cost-effective electrolysis systems.

Fe_2O_3 in SOEC: The integration of Fe_2O_3 to a samarium-doped ceria (SDC) interlayer in SOEC systems improves the ionic conductivity of the cathode electrode. The introduction of Fe_2O_3 as an interlayer dopant improves the cathode electrode stability and hydrogen production. More dedicated research in this direction could provide new insights regarding the applicability of Fe_2O_3 in high-temperature electrolysis.

7. Summary and Outlook

The discussion presented in this review offers an important and underlying strategy regarding the use of Fe_2O_3 in electrocatalytic water splitting systems. Among the explored metal oxides, hematite provides the most cost-effective and efficient option for electrolysis applications. The abundance, non-toxicity, cost, and stability of basic electrolytes are the main advantages of Fe_2O_3 electrodes compared to other oxide counterparts. Thus, Fe_2O_3 offers enormous potential in future energy devices due to its versatile applicability. However, the intrinsic properties of Fe_2O_3 limit its application as an efficient catalyst. Despite its wider pertinence in photoelectrochemical water splitting applications, its implementation in electrolysis is limited; it is nonetheless a promising option, and thus, novel strategies in this direction are essential.

In electrolysis, Fe_2O_3 is widely used as an OER catalyst, in addition to bifunctional and HER catalysts, when combined with suitable materials and following the application of suitable modifications. The most common modification strategies applied to Fe_2O_3 include crystal facet and morphology tuning, doping, the creation of multijunction systems (anchoring with other materials), use with carbon supports, MOF linking, seawater electrolysis, the use of the magnetic field effect, and the application of AEMWE and SOEC systems. The various modifications implemented with Fe_2O_3 offer a wide range of advantages that benefit its OER, HER, and/or bifunctional characteristics. In light of this, the discussion presented here provides a comprehensive summary of advancements regarding the use of Fe_2O_3 catalysts with different modifications. Each modification provides unique changes and improvements in Fe_2O_3 to improve its capabilities. For example, Fe_2O_3 combined with Fe_2Se_3 or Ni_3S_2/N-doped carbon NiO shows the lowest overpotential (+160 and +188 mV) ever reported for the Fe_2O_3 in 1 M KOH, generating an OER current density of 20 and 52 mA cm^{-2}, whereas Co-Fe_2O_3 shows exceptional stability of over 500 h when utilized in AEMWE systems. Despite its excellent performance in water splitting, reports addressing its use in electrolysis are limited when compared with those for other oxides. Therefore, significant research is essential to realize the full potential of Fe_2O_3 as a cost-effective and efficient water-splitting catalyst. Until now, the main focus has been in the direction of multijunction systems, whereas the doping strategy, facet tuning, and magnetic field effects have been rarely discussed. Therefore, a more significant focus in these directions could open up further potential of Fe_2O_3 as an efficient water-splitting catalyst. The thorough discussion on Fe_2O_3 presented here offers a solid platform for future research regarding the extensive modifications required to develop a highly efficient, stable, and cheap catalyst for electrocatalytic OER and HER. Importantly, the valuable insights presented here will offer detailed guidelines for the efficient design of Fe_2O_3-based catalysis systems.

Author Contributions: S.S.K.: writing—original draft preparation, writing—review and editing. B.G.P.: writing—review and editing, supervision, funding acquisition. All authors have read and agreed to the published version of the manuscript.

Funding: This research received no external funding.

Institutional Review Board Statement: Not applicable.

Informed Consent Statement: Not applicable.

Data Availability Statement: Data are contained within the article.

Acknowledgments: The researchers at the Green Hydrogen Lab (UQTR Hydrogen Research Institute) would like to acknowledge the support of the Natural Sciences and Engineering Research Council of Canada (NSERC) Tier 1 Canada Research Chair in Green Hydrogen Production, the Québec Ministère de l'Économie, de l'Innovation et de l'Énergie (MEIE) [Développement de catalyseurs et d'électrodes innovants, à faibles coûts, performants et durables pour la production d'hydrogène vert, funding reference number 00393501], and Innergex Renewable Energy Inc. for the Innergex Research Chair in Renewable Hydrogen Production.

Conflicts of Interest: The authors declare no conflict of interest.

References

1. Asafu-Adjaye, J.; Byrne, D.; Alvarez, M. Economic Growth, Fossil Fuel and Non-Fossil Consumption: A Pooled Mean Group Analysis Using Proxies for Capital. *Energy Econ.* **2016**, *60*, 345–356. [CrossRef]
2. Bildirici, M.E.; Bakirtas, T. The Relationship among Oil, Natural Gas and Coal Consumption and Economic Growth in BRICTS (Brazil, Russian, India, China, Turkey and South Africa) Countries. *Energy* **2014**, *65*, 134–144. [CrossRef]
3. Zhang, X.; Li, J.-R. Recovery of Greenhouse Gas as Cleaner Fossil Fuel Contributes to Carbon Neutrality. *Green Energy Environ.* **2023**, *8*, 351–353. [CrossRef]
4. Bölük, G.; Mert, M. Fossil & Renewable Energy Consumption, GHGs (Greenhouse Gases) and Economic Growth: Evidence from a Panel of EU (European Union) Countries. *Energy* **2014**, *74*, 439–446. [CrossRef]
5. Momirlan, M.; Veziroglu, T.N. The Properties of Hydrogen as Fuel Tomorrow in Sustainable Energy System for a Cleaner Planet. *Int. J. Hydrog. Energy* **2005**, *30*, 795–802. [CrossRef]
6. Armaroli, N.; Balzani, V. The Hydrogen Issue. *ChemSusChem* **2011**, *4*, 21–36. [CrossRef]
7. Oshiro, K.; Fujimori, S. Role of Hydrogen-Based Energy Carriers as an Alternative Option to Reduce Residual Emissions Associated with Mid-Century Decarbonization Goals. *Appl. Energy* **2022**, *313*, 118803. [CrossRef]
8. Haram, M.H.S.M.; Lee, J.W.; Ramasamy, G.; Ngu, E.E.; Thiagarajah, S.P.; Lee, Y.H. Feasibility of Utilising Second Life EV Batteries: Applications, Lifespan, Economics, Environmental Impact, Assessment, and Challenges. *Alex. Eng. J.* **2021**, *60*, 4517–4536. [CrossRef]
9. Gao, Y.; Zhu, C.; Zhang, X.; Guo, B. Implementation and Evaluation of a Practical Electrochemical- Thermal Model of Lithium-Ion Batteries for EV Battery Management System. *Energy* **2021**, *221*, 119688. [CrossRef]
10. Yang, Z.; Huang, H.; Lin, F. Sustainable Electric Vehicle Batteries for a Sustainable World: Perspectives on Battery Cathodes, Environment, Supply Chain, Manufacturing, Life Cycle, and Policy. *Adv. Energy Mater.* **2022**, *12*, 2200383. [CrossRef]
11. Robiou du Pont, Y.; Jeffery, M.L.; Gütschow, J.; Rogelj, J.; Christoff, P.; Meinshausen, M. Equitable Mitigation to Achieve the Paris Agreement Goals. *Nat. Clim Chang.* **2017**, *7*, 38–43. [CrossRef]
12. Katebah, M.; Al-Rawashdeh, M.; Linke, P. Analysis of Hydrogen Production Costs in Steam-Methane Reforming Considering Integration with Electrolysis and CO_2 Capture. *Clean. Eng. Technol.* **2022**, *10*, 100552. [CrossRef]
13. Trasatti, S. Water Electrolysis: Who First? *J. Electroanal. Chem.* **1999**, *476*, 90–91. [CrossRef]
14. Swierk, J.R.; Klaus, S.; Trotochaud, L.; Bell, A.T.; Tilley, T.D. Electrochemical Study of the Energetics of the Oxygen Evolution Reaction at Nickel Iron (Oxy)Hydroxide Catalysts. *J. Phys. Chem. C* **2015**, *119*, 19022–19029. [CrossRef]
15. Xue, Y.; Wang, Y. A Review of the α-Fe_2O_3 (Hematite) Nanotube Structure: Recent Advances in Synthesis, Characterization, and Applications. *Nanoscale* **2020**, *12*, 10912–10932. [CrossRef] [PubMed]
16. Jung, J.-W.; Jang, J.-S.; Yun, T.G.; Yoon, K.R.; Kim, I.-D. Three-Dimensional Nanofibrous Air Electrode Assembled with Carbon Nanotubes-Bridged Hollow Fe_2O_3 Nanoparticles for High-Performance Lithium–Oxygen Batteries. *ACS Appl. Mater. Interfaces* **2018**, *10*, 6531–6540. [CrossRef]
17. Nithya, V.D.; Arul, N.S. Review on α-Fe_2O_3 Based Negative Electrode for High Performance Supercapacitors. *J. Power Sources* **2016**, *327*, 297–318. [CrossRef]
18. Wang, H.; Luo, Y.; Li, K.; Liu, B.; Gao, L.; Duan, G. Porous α-Fe_2O_3 Gas Sensor with Instantaneous Attenuated Response toward Triethylamine and Its Reaction Kinetics. *Chem. Eng. J.* **2022**, *427*, 131631. [CrossRef]
19. Meenakshi, S.; Anitta, S.; Sivakumar, A.; Martin Britto Dhas, S.A.; Sekar, C. Shock Waves Exposed α-Fe_2O_3 Nanoparticles for Electrochemical Sensing of Riboflavin, Uric Acid and Folic Acid. *Microchem. J.* **2021**, *168*, 106403. [CrossRef]
20. Makimizu, Y.; Nguyen, N.T.; Tucek, J.; Ahn, H.-J.; Yoo, J.; Poornajar, M.; Hwang, I.; Kment, S.; Schmuki, P. Activation of α-Fe_2O_3 for Photoelectrochemical Water Splitting Strongly Enhanced by Low Temperature Annealing in Low Oxygen Containing Ambient. *Chem. A Eur. J.* **2020**, *26*, 2685–2692. [CrossRef]
21. Fawzi Suleiman Khasawneh, O.; Palaniandy, P. Removal of Organic Pollutants from Water by Fe_2O_3/TiO_2 Based Photocatalytic Degradation: A Review. *Environ. Technol. Innov.* **2021**, *21*, 101230. [CrossRef]
22. Dash, P.; Raut, S.; Jena, M.; Nayak, B. Harnessing the Biomedical Properties of Ferromagnetic α-Fe_2O_3 NPs with a Plausible Formation Mechanism. *Ceram. Int.* **2020**, *46*, 26190–26204. [CrossRef]
23. Damizia, M.; Lloreda-Jurado, P.J.; De Filippis, P.; de Caprariis, B.; Chicardi, E.; Sepúlveda, R. Green Hydrogen Production Using Doped Fe_2O_3 Foams. *Int. J. Hydrog. Energy* **2024**, *51*, 834–845. [CrossRef]
24. Hu, C.; Li, X.; Dong, C.; Li, B.; Zhang, X.; Sun, W.; Ding, Y. Key Modification Strategies for the Rational Design of Hematite to Promote Photoelectrochemical Water Oxidation: A Review of Recent Advances. *Mater. Chem. Front.* **2023**, *7*, 5333–5354. [CrossRef]
25. Zuo, Y.; Mastronardi, V.; Gamberini, A.; Zappia, M.I.; Le, T.-H.-H.; Prato, M.; Dante, S.; Bellani, S.; Manna, L. Stainless Steel Activation for Efficient Alkaline Oxygen Evolution in Advanced Electrolyzers. *Adv. Mater.* **2024**, *36*, 2312071. [CrossRef]
26. Wang, P.C.; Ding, H.P.; Bark, T.; Chen, C.H. Nanosized α-Fe_2O_3 and Li–Fe Composite Oxide Electrodes for Lithium-Ion Batteries. *Electrochim. Acta* **2007**, *52*, 6650–6655. [CrossRef]
27. Kusano, Y.; Fukuhara, M.; Takada, J.; Doi, A.; Ikeda, Y.; Takano, M. Science in the Art of the Master Bizen Potter. *Acc. Chem. Res.* **2010**, *43*, 906–915. [CrossRef]
28. Han, Y.S.; Yun, S.M.; Kim, D.G. Synthesis of Monodispersed and Spherical SiO_2-Coated Fe_2O_3 Nanoparticle. *Bull. Korean Chem. Soc.* **2000**, *21*, 1193–1198. [CrossRef]

29. Danno, T.; Nakatsuka, D.; Kusano, Y.; Asaoka, H.; Nakanishi, M.; Fujii, T.; Ikeda, Y.; Takada, J. Crystal Structure of β-Fe_2O_3 and Topotactic Phase Transformation to α-Fe_2O_3. *Cryst. Growth Des.* **2013**, *13*, 770–774. [CrossRef]
30. Tuček, J.; Zbořil, R.; Namai, A.; Ohkoshi, S. ε-Fe_2O_3: An Advanced Nanomaterial Exhibiting Giant Coercive Field, Millimeter-Wave Ferromagnetic Resonance, and Magnetoelectric Coupling. *Chem. Mater.* **2010**, *22*, 6483–6505. [CrossRef]
31. Pourmadadi, M.; Rahmani, E.; Shamsabadipour, A.; Mahtabian, S.; Ahmadi, M.; Rahdar, A.; Díez-Pascual, A.M. Role of Iron Oxide (Fe_2O_3) Nanocomposites in Advanced Biomedical Applications: A State-of-the-Art Review. *Nanomaterials* **2022**, *12*, 3873. [CrossRef] [PubMed]
32. Momma, K.; Izumi, F. VESTA 3 for Three-Dimensional Visualization of Crystal, Volumetric and Morphology Data. *J. Appl. Cryst.* **2011**, *44*, 1272–1276. [CrossRef]
33. Wu, H.; Yang, T.; Du, Y.; Shen, L.; Ho, G.W. Identification of Facet-Governing Reactivity in Hematite for Oxygen Evolution. *Adv. Mater.* **2018**, *30*, 1804341. [CrossRef]
34. Xiao, M.; Xing, Z.; Jin, Z.; Liu, C.; Ge, J.; Zhu, J.; Wang, Y.; Zhao, X.; Chen, Z. Preferentially Engineering FeN4 Edge Sites onto Graphitic Nanosheets for Highly Active and Durable Oxygen Electrocatalysis in Rechargeable Zn–Air Batteries. *Adv. Mater.* **2020**, *32*, 2004900. [CrossRef]
35. Chen, J.; Li, H.; Fan, C.; Meng, Q.; Tang, Y.; Qiu, X.; Fu, G.; Ma, T. Dual Single-Atomic Ni-N4 and Fe-N4 Sites Constructing Janus Hollow Graphene for Selective Oxygen Electrocatalysis. *Adv. Mater.* **2020**, *32*, 2003134. [CrossRef] [PubMed]
36. Li, F.-L.; Shao, Q.; Huang, X.; Lang, J.-P. Nanoscale Trimetallic Metal–Organic Frameworks Enable Efficient Oxygen Evolution Electrocatalysis. *Angew. Chem. Int. Ed.* **2018**, *57*, 1888–1892. [CrossRef]
37. Li, M.; Ye, K.-H.; Qiu, W.; Wang, Y.; Ren, H. Heterogeneity between and within Single Hematite Nanorods as Electrocatalysts for Oxygen Evolution Reaction. *J. Am. Chem. Soc.* **2022**, *144*, 5247–5252. [CrossRef]
38. Kalanur, S.S.; Lee, Y.J.; Seo, H. A Versatile Synthesis Strategy and Band Insights of Monoclinic Clinobisvanite $BiVO_4$ Thin Films for Enhanced Photoelectrochemical Water Splitting Activity. *Appl. Surf. Sci.* **2021**, *562*, 150078. [CrossRef]
39. Nguyën, H.C.; Garcés-Pineda, F.A.; de Fez-Febré, M.; Galán-Mascarós, J.R.; López, N. Non-Redox Doping Boosts Oxygen Evolution Electrocatalysis on Hematite. *Chem. Sci.* **2020**, *11*, 2464–2471. [CrossRef]
40. Shah, S.A.; Zhu, G.; Yuan, A.; Ullah, N.; Shen, X.; Khan, H.; Xu, K.; Wang, X.; Yan, X. Loading of Individual Se-Doped Fe_2O_3-Decorated Ni/NiO Particles on Carbon Cloth: Facile Synthesis and Efficient Electrocatalysis for the Oxygen Evolution Reaction. *Dalton Trans.* **2020**, *49*, 15682–15692. [CrossRef]
41. Zhang, X.-Y.; Li, F.-T.; Fan, R.-Y.; Zhao, J.; Dong, B.; Wang, F.-L.; Liu, H.-J.; Yu, J.-F.; Liu, C.-G.; Chai, Y.-M. F, P Double-Doped Fe3O4 with Abundant Defect Sites for Efficient Hydrogen Evolution at High Current Density. *J. Mater. Chem. A* **2021**, *9*, 15836–15845. [CrossRef]
42. Ganje, P.M.; Bandal, H.A.; Kim, H. Free-Standing P-Doped Fe_2O_3/ZnO Nanotubes as a Bifunctional Electrocatalyst for Electrochemical Water Splitting. *Sustain. Energy Fuels* **2022**, *6*, 5579–5590. [CrossRef]
43. Haschke, S.; Pankin, D.; Petrov, Y.; Bochmann, S.; Manshina, A.; Bachmann, J. Design Rules for Oxygen Evolution Catalysis at Porous Iron Oxide Electrodes: A 1000-Fold Current Density Increase. *ChemSusChem* **2017**, *10*, 3644–3651. [CrossRef]
44. Zhang, J.; Shang, X.; Ren, H.; Chi, J.; Fu, H.; Dong, B.; Liu, C.; Chai, Y. Modulation of Inverse Spinel Fe3O4 by Phosphorus Doping as an Industrially Promising Electrocatalyst for Hydrogen Evolution. *Adv. Mater.* **2019**, *31*, 1905107. [CrossRef]
45. Liu, H.-J.; Zhang, S.; Yang, W.-Y.; Yu, N.; Liu, C.-Y.; Chai, Y.-M.; Dong, B. Directional Reconstruction of Iron Oxides to Active Sites for Superior Water Oxidation. *Adv. Funct. Mater.* **2023**, *33*, 2303776. [CrossRef]
46. Ng, K.-L.; Kok, K.-Y.; Ong, B.-H. Facile Synthesis of Self-Assembled Cobalt Oxide Supported on Iron Oxide as the Novel Electrocatalyst for Enhanced Electrochemical Water Electrolysis. *ACS Appl. Nano Mater.* **2018**, *1*, 401–409. [CrossRef]
47. Farooq, A.; Khalil, S.; Basha, B.; Habib, A.; Al-Buriahi, M.S.; Warsi, M.F.; Yousaf, S.; Shahid, M. Electrochemical Investigation of C-Doped $CoFe_2O_4$/Fe_2O_3 Nanostructures for Efficient Electrochemical Water Splitting. *Int. J. Hydrog. Energy* **2024**, *51*, 1318–1332. [CrossRef]
48. Tong, H.; Zheng, X.; Qi, M.; Li, D.; Zhu, J.; Jiang, D. Synergistically Coupled CoMo/Fe_2O_3 Electrocatalyst for Highly Efficient and Stable Overall Water Splitting. *J. Colloid Interface Sci.* **2024**, *676*, 837–846. [CrossRef]
49. Alothman, A.A.; Shah, J.H.; Aljadoa, K.A.; Soykan, G.; Yalçin, Ş.; Abid, A.G.; Allakhverdiev, S.I. Fabrication of Heterojunction Electrode Based on Fe_2O_3@CuO-400 Nanocomposite Constructed for Hydrogen Production. *Int. J. Hydrog. Energy* **2024**, *61*, 1004–1014. [CrossRef]
50. Yang, X.; Li, Y.; Deng, L.; Li, W.; Ren, Z.; Yang, M.; Yang, X.; Zhu, Y. Synthesis and Characterization of an IrO_2–Fe_2O_3 Electrocatalyst for the Hydrogen Evolution Reaction in Acidic Water Electrolysis. *RSC Adv.* **2017**, *7*, 20252–20258. [CrossRef]
51. Mosallaei, H.; Hadadzadeh, H.; Foelske, A.; Sauer, M.; Rudbari, H.A.; Blacque, O. $[Ru(Tmphen)_3]_2[Fe(CN)_6]$ and $[Ru(Phen)_3][Fe(CN)_5(NO)]$ Complexes and Formation of a Heterostructured RuO_2–Fe_2O_3 Nanocomposite as an Efficient Alkaline HER and OER Electrocatalyst. *Dalton Trans.* **2022**, *51*, 6314–6331. [CrossRef] [PubMed]
52. Mosallaei, H.; Hadadzadeh, H.; Ensafi, A.A.; Mousaabadi, K.Z.; Weil, M.; Foelske, A.; Sauer, M. Evaluation of HER and OER Electrocatalytic Activity over RuO_2–Fe_2O_3 Nanocomposite Deposited on HrGO Nanosheets. *Int. J. Hydrog. Energy* **2023**, *48*, 1813–1830. [CrossRef]
53. Sang, Y.; Cao, X.; Ding, G.; Guo, Z.; Xue, Y.; Li, G.; Yu, R. Constructing Oxygen Vacancy-Enriched Fe_2O_3@NiO Heterojunctions for Highly Efficient Electrocatalytic Alkaline Water Splitting. *CrystEngComm* **2021**, *24*, 199–207. [CrossRef]

54. Xiao, X.; Ma, R.; Li, D.; Yang, M.; Tong, Y.; Qiu, Z.; Jing, B.; Yang, T.; Hu, R.; Yang, Y.; et al. Tungsten Oxide Decorating-Regulated Iron-Nickel Oxide Heterostructure as Electrocatalyst for Oxygen Evolution Reaction. *J. Alloys Compd.* **2023**, *968*, 171910. [CrossRef]
55. Kong, A.; Zhang, H.; Sun, Y.; Lv, Y.; Liu, M.; Li, H.; Wang, Y.; Fu, Y.; Zhang, H.; Li, W.; et al. Surface Reconstruction Enables Outstanding Performance of Fe_2O_3/$Ni(OH)_2$ Nanosheet Arrays for Ultrahigh Current Density Oxygen Evolution Reaction. *Appl. Surf. Sci.* **2023**, *613*, 156023. [CrossRef]
56. Xue, Y.; Zhang, X.; Yao, J.; Zhao, J.; Xu, Y.; Yan, Q.; Ye, K.; Zhu, K.; Cao, D.; Wang, G. Ultrathin Fe_2O_3 Shell-Encapsulated NiFe Alloy Nanoparticles Embedded in Tubular Carbon Matrix for Enhanced Oxygen Evolution Reaction. *J. Alloys Compd.* **2023**, *935*, 167922. [CrossRef]
57. Kim, J.; Heo, J.N.; Do, J.Y.; Chava, R.K.; Kang, M. Electrochemical Synergies of Heterostructured Fe_2O_3-MnO Catalyst for Oxygen Evolution Reaction in Alkaline Water Splitting. *Nanomaterials* **2019**, *9*, 1486. [CrossRef]
58. Wang, Y.; Chen, Z.; Wu, H.; Xiao, F.; Cao, E.; Du, S.; Wu, Y.; Ren, Z. Self-Assembly-Induced Mosslike Fe_2O_3 and FeP on Electro-Oxidized Carbon Paper for Low-Voltage-Driven Hydrogen Production Plus Hydrazine Degradation. *ACS Sustain. Chem. Eng.* **2018**, *6*, 15727–15736. [CrossRef]
59. Ahmad, I.; Ahmed, J.; Batool, S.; Zafar, M.N.; Hanif, A.; Zahidullah; Nazar, M.F.; Ul-Hamid, A.; Jabeen, U.; Dahshan, A.; et al. Design and Fabrication of Fe_2O_3/FeP Heterostructure for Oxygen Evolution Reaction Electrocatalysis. *J. Alloys Compd.* **2022**, *894*, 162409. [CrossRef]
60. Khan, N.A.; Rashid, N.; Ahmad, I.; Zahidullah; Zairov, R.; ur Rehman, H.; Nazar, M.F.; Jabeen, U. An Efficient Fe_2O_3/FeS Heterostructures Water Oxidation Catalyst. *Int. J. Hydrog. Energy* **2022**, *47*, 22340–22347. [CrossRef]
61. Guo, W.H.; Zhang, Q.; Fu, H.C.; Yang, Y.X.; Chen, X.H.; Luo, H.Q.; Li, N.B. Semi-Sacrificial Template Growth of FeS/Fe_2O_3 Heterogeneous Nanosheets on Iron Foam for Efficient Oxygen Evolution Reaction. *J. Alloys Compd.* **2022**, *909*, 164670. [CrossRef]
62. Sohail, M.; Ayyob, M.; Wang, A.; Sun, Z.; El Maati, L.A.; Altuijri, R.; Zairov, R.; Ahmad, I. An Efficient Fe_2Se_3/Fe_2O_3 Heterostructure Electrocatalyst for Oxygen Evolution Reaction. *Int. J. Hydrog. Energy* **2024**, *52*, 1290–1297. [CrossRef]
63. Haschke, S.; Wu, Y.; Bashouti, M.; Christiansen, S.; Bachmann, J. Engineering Nanoporous Iron(III) Oxide into an Effective Water Oxidation Electrode. *ChemCatChem* **2015**, *7*, 2455–2459. [CrossRef]
64. Yuan, W.; Zhao, M.; Yuan, J.; Li, C.M. Ni Foam Supported Three-Dimensional Vertically Aligned and Networked Layered CoO Nanosheet/Graphene Hybrid Array as a High-Performance Oxygen Evolution Electrode. *J. Power Sources* **2016**, *319*, 159–167. [CrossRef]
65. Cheng, H.; Su, Y.-Z.; Kuang, P.-Y.; Chen, G.-F.; Liu, Z.-Q. Hierarchical $NiCo_2O_4$ Nanosheet-Decorated Carbon Nanotubes towards Highly Efficient Electrocatalyst for Water Oxidation. *J. Mater. Chem. A* **2015**, *3*, 19314–19321. [CrossRef]
66. Kargar, A.; Yavuz, S.; Kim, T.K.; Liu, C.-H.; Kuru, C.; Rustomji, C.S.; Jin, S.; Bandaru, P.R. Solution-Processed $CoFe_2O_4$ Nanoparticles on 3D Carbon Fiber Papers for Durable Oxygen Evolution Reaction. *ACS Appl. Mater. Interfaces* **2015**, *7*, 17851–17856. [CrossRef]
67. Bandal, H.A.; Jadhav, A.R.; Chaugule, A.A.; Chung, W.-J.; Kim, H. Fe_2O_3 Hollow Nanorods/CNT Composites as an Efficient Electrocatalyst for Oxygen Evolution Reaction. *Electrochim. Acta* **2016**, *222*, 1316–1325. [CrossRef]
68. Zang, Y.; Zhang, H.; Zhang, X.; Liu, R.; Liu, S.; Wang, G.; Zhang, Y.; Zhao, H. Fe/Fe_2O_3 Nanoparticles Anchored on Fe-N-Doped Carbon Nanosheets as Bifunctional Oxygen Electrocatalysts for Rechargeable Zinc-Air Batteries. *Nano Res.* **2016**, *9*, 2123–2137. [CrossRef]
69. Alduhaish, O.; Ubaidullah, M.; Al-Enizi, A.M.; Alhokbany, N.; Alshehri, S.M.; Ahmed, J. Facile Synthesis of Mesoporous α-Fe_2O_3@g-C_3N_4-NCs for Efficient Bifunctional Electro-Catalytic Activity (OER/ORR). *Sci Rep* **2019**, *9*, 14139. [CrossRef]
70. Jiang, J.; Zhu, L.; Sun, Y.; Chen, Y.; Chen, H.; Han, S.; Lin, H. Fe_2O_3 Nanocatalysts on N-Doped Carbon Nanomaterial for Highly Efficient Electrochemical Hydrogen Evolution in Alkaline. *J. Power Sources* **2019**, *426*, 74–83. [CrossRef]
71. Shah, S.A.; Shen, X.; Yuan, A.; Ji, Z.; Yue, X.; Zhu, G.; Zhou, H.; Xu, K.; Zhu, J.; Chen, Y. One Step In-Situ Synthesis of Ni_3S_2/Fe_2O_3/N-Doped Carbon Composites on Ni Foam as an Efficient Electrocatalyst for Overall Water Splitting. *Appl. Surf. Sci.* **2020**, *527*, 146918. [CrossRef]
72. Mousavi, D.S.; Shahrokhian, S.; Iraji zad, A. Sugar-Cubic Fe_2O_3/Nitrogen-Doped Graphene Nanocomposite as High-Performance Anode Material for Oxygen Evolution Reaction. *J. Alloys Compd.* **2022**, *910*, 164852. [CrossRef]
73. Kang, S.; Lee, K.; Ryu, J.H.; Ali, G.; Akbar, M.; Chung, K.Y.; Chung, C.-Y.; Han, H.; Kim, K.M. Transition Metal Compounds on Functionalized Multiwall Carbon Nanotubes for the Efficient Oxygen Evolution Reaction. *ACS Appl. Nano Mater.* **2023**, *6*, 4319–4327. [CrossRef]
74. Zhang, H.; Nai, J.; Yu, L.; Lou, X.W. (David) Metal-Organic-Framework-Based Materials as Platforms for Renewable Energy and Environmental Applications. *Joule* **2017**, *1*, 77–107. [CrossRef]
75. Niu, Y.; Yuan, Y.; Zhang, Q.; Chang, F.; Yang, L.; Chen, Z.; Bai, Z. Morphology-Controlled Synthesis of Metal-Organic Frameworks Derived Lattice Plane-Altered Iron Oxide for Efficient Trifunctional Electrocatalysts. *Nano Energy* **2021**, *82*, 105699. [CrossRef]
76. Song, H.J.; Yoon, H.; Ju, B.; Lee, D.-Y.; Kim, D.-W. Electrocatalytic Selective Oxygen Evolution of Carbon-Coated $Na_2Co_{1-x}FexP_2O_7$ Nanoparticles for Alkaline Seawater Electrolysis. *ACS Catal.* **2020**, *10*, 702–709. [CrossRef]
77. Miao, J.; Lang, Z.; Zhang, X.; Kong, W.; Peng, O.; Yang, Y.; Wang, S.; Cheng, J.; He, T.; Amini, A.; et al. Polyoxometalate-Derived Hexagonal Molybdenum Nitrides (MXenes) Supported by Boron, Nitrogen Codoped Carbon Nanotubes for Efficient Electrochemical Hydrogen Evolution from Seawater. *Adv. Funct. Mater.* **2019**, *29*, 1805893. [CrossRef]

78. Wang, C.; Zhu, M.; Cao, Z.; Zhu, P.; Cao, Y.; Xu, X.; Xu, C.; Yin, Z. Heterogeneous Bimetallic Sulfides Based Seawater Electrolysis towards Stable Industrial-Level Large Current Density. *Appl. Catal. B Environ.* **2021**, *291*, 120071. [CrossRef]
79. Li, L.; Zhang, G.; Wang, B.; Zhu, D.; Liu, D.; Liu, Y.; Yang, S. Fe_2O_3/NiO Interface for the Electrochemical Oxygen Evolution in Seawater and Domestic Sewage. *ACS Appl. Mater. Interfaces* **2021**, *13*, 37152–37161. [CrossRef]
80. Cui, T.; Zhai, X.; Guo, L.; Chi, J.-Q.; Zhang, Y.; Zhu, J.; Sun, X.; Wang, L. Controllable Synthesis of a Self-Assembled Ultralow Ru, Ni-Doped Fe_2O_3 Lily as a Bifunctional Electrocatalyst for Large-Current-Density Alkaline Seawater Electrolysis. *Chin. J. Catal.* **2022**, *43*, 2202–2211. [CrossRef]
81. Cui, Z.; Yan, Z.; Yin, J.; Wang, W.; Yue, M.-E.; Li, Z. Engineering P-Fe_2O_3-CoP Nanosheets for Overall Freshwater and Seawater Splitting. *J. Colloid Interface Sci.* **2023**, *652*, 1117–1125. [CrossRef] [PubMed]
82. Koza, J.A.; Uhlemann, M.; Gebert, A.; Schultz, L. Desorption of Hydrogen from the Electrode Surface under Influence of an External Magnetic Field. *Electrochem. Commun.* **2008**, *10*, 1330–1333. [CrossRef]
83. Koza, J.A.; Mühlenhoff, S.; Żabiński, P.; Nikrityuk, P.A.; Eckert, K.; Uhlemann, M.; Gebert, A.; Weier, T.; Schultz, L.; Odenbach, S. Hydrogen Evolution under the Influence of a Magnetic Field. *Electrochim. Acta* **2011**, *56*, 2665–2675. [CrossRef]
84. Yan, J.; Wang, Y.; Zhang, Y.; Xia, S.; Yu, J.; Ding, B. Direct Magnetic Reinforcement of Electrocatalytic ORR/OER with Electromagnetic Induction of Magnetic Catalysts. *Adv. Mater.* **2021**, *33*, 2007525. [CrossRef] [PubMed]
85. Luo, S.; Elouarzaki, K.; Xu, Z.J. Electrochemistry in Magnetic Fields. *Angew. Chem. Int. Ed.* **2022**, *61*, e202203564. [CrossRef] [PubMed]
86. Zhang, Y.; Liang, C.; Wu, J.; Liu, H.; Zhang, B.; Jiang, Z.; Li, S.; Xu, P. Recent Advances in Magnetic Field-Enhanced Electrocatalysis. *ACS Appl. Energy Mater.* **2020**, *3*, 10303–10316. [CrossRef]
87. Dastafkan, K.; Meyer, Q.; Chen, X.; Zhao, C. Efficient Oxygen Evolution and Gas Bubble Release Achieved by a Low Gas Bubble Adhesive Iron–Nickel Vanadate Electrocatalyst. *Small* **2020**, *16*, 2002412. [CrossRef]
88. Zhao, X.; Ren, H.; Luo, L. Gas Bubbles in Electrochemical Gas Evolution Reactions. *Langmuir* **2019**, *35*, 5392–5408. [CrossRef]
89. Li, X.; Hao, C.; Du, Y.; Lu, Y.; Fan, Y.; Wang, M.; Wang, N.; Meng, R.; Wang, X.; Xu, Z.J.; et al. Harnessing Magnetic Fields to Accelerate Oxygen Evolution Reaction. *Chin. J. Catal.* **2023**, *55*, 191–199. [CrossRef]
90. Saravanan, P.; Hsu, J.-H.; Sivaprahasam, D.; Kamat, S.V. Structural and Magnetic Properties of γ-Fe_2O_3 Nanostructured Compacts Processed by Spark Plasma Sintering. *J. Magn. Magn. Mater.* **2013**, *346*, 175–177. [CrossRef]
91. Chen, H.-Y.; Chen, G.-C.; Liao, K.-W.; Wei, W.-H.; Huang, H.-C.; Wang, C.-H. Island-Type Hybrid Catalysts Applied for Anion Exchange Membrane Water Electrolysis. *Catalysts* **2022**, *12*, 102. [CrossRef]
92. Lahrichi, A.; El Issmaeli, Y.; Kalanur, S.S.; Pollet, B.G. Advancements, Strategies, and Prospects of Solid Oxide Electrolysis Cells (SOECs): Towards Enhanced Performance and Large-Scale Sustainable Hydrogen Production. *J. Energy Chem.* **2024**, *94*, 688–715. [CrossRef]
93. Choi, H.-J.; Na, Y.-H.; Kwak, M.; Kim, T.W.; Seo, D.-W.; Woo, S.-K.; Kim, S.-D. Development of Solid Oxide Cells by Co-Sintering of GDC Diffusion Barriers with LSCF Air Electrode. *Ceram. Int.* **2017**, *43*, 13653–13660. [CrossRef]
94. Shimura, K.; Nishino, H.; Kakinuma, K.; Brito, M.E.; Uchida, H. Effect of Samaria-Doped Ceria (SDC) Interlayer on the Performance of $La_{0.6}Sr_{0.4}Co_{0.2}Fe_{0.8}O_{3-\delta}$/SDC Composite Oxygen Electrode for Reversible Solid Oxide Fuel Cells. *Electrochim. Acta* **2017**, *225*, 114–120. [CrossRef]
95. Zhang, T.S.; Ma, J.; Kong, L.B.; Chan, S.H.; Hing, P.; Kilner, J.A. Iron Oxide as an Effective Sintering Aid and a Grain Boundary Scavenger for Ceria-Based Electrolytes. *Solid State Ion.* **2004**, *167*, 203–207. [CrossRef]
96. Avila-Paredes, H.J.; Kim, S. The Effect of Segregated Transition Metal Ions on the Grain Boundary Resistivity of Gadolinium Doped Ceria: Alteration of the Space Charge Potential. *Solid State Ion.* **2006**, *177*, 3075–3080. [CrossRef]
97. Zhang, T.S.; Ma, J.; Leng, Y.J.; He, Z.M. Sintering, Microstructure and Grain Growth of Fe-Doped Ce0.9Gd0.1O2$-\delta$ Ceramics Derived from Oxalate Coprecipitation. *J. Cryst. Growth* **2005**, *274*, 603–611. [CrossRef]
98. Qu, Y.; Yu, J.; Tian, N.; Shen, H. Improved Performance of a Samarium-Doped Ceria Interlayer of Intermediate Temperature Solid Oxide Electrolysis Cells by Doping the Transition Metal Oxide Fe_2O_3. *RSC Adv.* **2021**, *11*, 30911–30917. [CrossRef]

Disclaimer/Publisher's Note: The statements, opinions and data contained in all publications are solely those of the individual author(s) and contributor(s) and not of MDPI and/or the editor(s). MDPI and/or the editor(s) disclaim responsibility for any injury to people or property resulting from any ideas, methods, instructions or products referred to in the content.